IEEE Access
Multidisciplinary ⋮ Rapid Review ⋮ Open Access Journal

Received 7 February 2025, accepted 23 March 2025, date of publication 27 March 2025, date of current version 7 April 2025.

Digital Object Identifier 10.1109/ACCESS.2025.3555518

RESEARCH ARTICLE

Winograd Transform-Based Fast Detection of Heart Disease Using ECG Signals and Chest X-Ray Images

RISHABH ANAND[1], ADYASHA RATH[1], (Student Member, IEEE), PRABODH KUMAR SAHOO[2], (Member, IEEE), PRINCE JAIN[2], (Member, IEEE), GANAPATI PANDA[3], (Life Senior Member, IEEE), XINHONG WANG[4], AND HAIPENG LIU[5]

[1]Department of Computer Science and Engineering, C. V. Raman Global University, Bhubaneswar, Odisha 752054, India
[2]Department of Mechatronics Engineering, Parul Institute of Technology, Parul University, Vadodara, Gujarat 391760, India
[3]Department of Electronics and Communication Engineering, C. V. Raman Global University, Bhubaneswar, Odisha 752054, India
[4]Department of Radiology, The Second Affiliated Hospital, Zhejiang University School of Medicine, Hangzhou, Zhejiang 310009, China
[5]Centre for Intelligent Healthcare, Coventry University, CV1 5RW Coventry, U.K.

Corresponding authors: Xinhong Wang (2611104@zju.edu.cn), Prince Jain (princeece48@gmail.com), and Prabodh Kumar Sahoo (sahooprabodhkumar@gmail.com)

This work was supported in part by Zhejiang Provincial Natural Science Foundation under Grant QN25H180024, and in part by the Medical Health Science and Technology Project of Zhejiang Provincial Health Commission under Grant 2024KY1036.

ABSTRACT In resource-constrained environments, efficient feature extraction is crucial for applications in classification and prediction tasks. This study investigates a fast, DFT-based, one-dimensional Winograd Transform (WT) to extract convolution-based features from 1-D ECG signals. For two-dimensional (2-D) Chest X-Ray (CXR) images, 2-D DFT-based convolution is employed to generate features. Traditional multi-stage convolution methods for feature extraction can be slow and computationally intensive. Therefore, to improve speed and accuracy in heart disease (HD) detection, WT-based convolution methods for both 1-D and 2-D data are applied to extract features from ECG signals and CXR images. These features serve as inputs for AI-based detection models, with six machine learning (ML) and four deep learning (DL) models developed for HD detection. Using standard datasets, extensive simulations were conducted, yielding various performance metrics that were analyzed and compared. Additionally, the feature extraction and model training times were evaluated and compared. The comparative analysis demonstrates that WT-based feature extraction significantly reduces processing time for both 1-D and 2-D data types. The WT-based method achieved speedups of x times for 1-D and y times for 2-D feature extraction relative to traditional convolution methods. Performance metrics, including classification accuracy (0.94) and AUC scores (0.98), remained consistently high across models, confirming that WT-based circular convolution offers a practical and effective solution for real-time heart disease detection. This approach enhances diagnostic capabilities in healthcare by enabling resource-efficient, real-time feature extraction in medical image and signal processing.

INDEX TERMS Circular convolution, discrete Fourier Transform (DFT), fast feature extraction, heart disease detection, Winograd Transform.

I. INTRODUCTION

THE rising prevalence of HD worldwide has necessitated the development of rapid and reliable diagnostic tools. Electrocardiogram (ECG) and Chest X-ray (CXR) imaging are foundational modalities in cardiovascular diagnostics, providing critical information on cardiac function and structural anomalies. However, modern diagnostic models relying on DL often require extensive feature extraction processes, which are computationally intensive and time-consuming.

The associate editor coordinating the review of this manuscript and approving it for publication was Gustavo Callico.

Traditional feature extraction methods, such as time-domain analysis and Fourier-based approaches, have proven effective but involve substantial computational resources, especially as data volumes grow. As a result, training these models can take hours, if not days, for large datasets; which limits their real-time application in clinical settings where timely diagnosis is essential.

Addressing this knowledge gap is crucial, as efficient feature extraction can significantly reduce computational time and cost, facilitating the broader application of DL models in low-resource settings. Current DL models, for example, Convolutional Neural Networks (CNNs) for ECG and CXR analysis, often suffer from high computational demands due to their reliance on these traditional methods. Despite notable advances in processing speed, the complexity of these models often remain beyond reach for many healthcare facilities, creating a need for optimized techniques that can deliver accuracy with improved speed [1].

This study proposes the introduction of the Winograd Transform (WT) based Circular Convolution method for an efficient extraction of features in DL models applied for HD detection. The WT offers a computationally efficient approach to perform convolution by reducing the number of arithmetic operations, particularly multiplications, required for feature extraction. This reduction enables faster training of models for classification or prediction task as well as faster inference times, which has the potential to transform DL applications in real-world medical diagnostics by making them more accessible and practical for clinical use. The following sections provide an in-depth review of pertinent literature, current approaches in ECG and CXR analysis, and the proposed benefits of adopting the WT in convolution-based DL models.

II. LITERATURE REVIEW

The global mortality rates for arrhythmia exhibit significant regional variations, influenced by factors such as healthcare access and lifestyle. According to the Global Burden of Disease Study, arrhythmias contribute notably to cardiovascular disease mortality, particularly in low and middle-income countries where the burden is disproportionately high [2]. Arrhythmias account for approximately 1.5 million deaths annually worldwide, with a higher prevalence in regions like sub-Saharan Africa and parts of Asia [3]. Though, in developed countries, mortality rates have decreased due to improved health care, in developing countries they are rising due to urbanization and lifestyle changes [3]. For example, while observing regional variations, eastern Europe and parts of Asia had the highest mortality rates, with significant increases in cardiovascular diseases, including arrhythmia, linked to lifestyle changes and healthcare disparities [4]. In contrast, North America and western Europe have seen substantial declines in mortality rates due to better management of cardiovascular risk factors [5]. Despite these trends, HD remains a critical public health issue globally, with ongoing challenges in prevention and treatment, particularly in resource-limited settings. Therefore, Early detection of HD plays a crucial role in reducing mortality rates and improving treatment outcomes. By identifying abnormal heart rhythms immediately, healthcare providers can implement timely interventions, thereby mitigating the risks associated with severe cardiac events.

Enhanced Monitoring Technologies Implantable Cardiac Stimulators integrate various therapies to detect and treat ventricular arrhythmias effectively. They adjust treatment aggressiveness based on heart rate and hemodynamic tolerance, which can prevent life-threatening situations [6]. Subcutaneous Implantable Cardioverter/Defibrillator systems monitor cardiac signals and analyze parameters like rate and QRS pulse width to determine when to deliver therapy, ensuring rapid response to arrhythmias [7]. Predictive Biomarkers Cardiotoxicity Detection: Advanced echocardiographic measurements and biomarkers, such as high-sensitivity cardiac troponin I, can predict cardiotoxicity in chemotherapy patients, allowing for early intervention and potentially reducing associated morbidity and mortality [8]. While early detection technologies show promise, challenges remain in ensuring widespread access and integration into standard care practices, which may limit their impact on overall mortality rates.

The diagnosis of HD in low-resource settings presents significant challenges, primarily due to the limited access to advanced diagnostic tools and trained healthcare professionals. The increasing burden of cardiovascular diseases, including arrhythmias, in low and middle-income countries (LMICs) exacerbates this problem, as there are few registries for electrophysiological disorders and their treatment [9]. Traditional methods of analyzing medical reports are often inefficient, requiring extensive manual supervision, which is not feasible in resource-limited environments [10]. Moreover, the reliance on outdated technologies and the lack of telemedicine infrastructure hinder timely and accurate diagnoses [9]. The development of AI and ML models, while promising, is still not widely implemented, leaving many patients without access to effective diagnostic solutions [11], [12]. Consequently, the integration of innovative technologies into healthcare systems is crucial to improve HD detection and management in these settings.

ECG is the most widely used modality for detecting arrhythmias in clinical research due to its simplicity, cost-effectiveness, and ability to provide real-time monitoring of heart activity. ECG signals, particularly the R peak, are crucial for diagnosing various heart conditions, including arrhythmias, which can be categorized into Tachycardia and Bradycardia for better identification [13]. It offers several advantages for HD detection compared to other methods like EEG, heart sounds, and magnetocardiogram (MCG). ECG is a widely used, non-invasive technique that provides real-time monitoring of the heart's electrical activity, making it effective for diagnosing various cardiac conditions [14]. Additionally, advancements in DL models have significantly

improved ECG analysis, enhancing diagnostic accuracy and enabling the detection of arrhythmias and other pathologies [15], [16]. However, ECG has limitations, such as its sensitivity to noise and the challenge of obtaining high-quality data, which can affect diagnostic performance [17]. In contrast, MCG can visualize cardiac electromagnetic activity and may provide complementary information, but it is less commonly used due to its complexity and the need for specialized equipment [18]. In general, while the ECG remains a cornerstone in cardiac diagnostics, integrating it with other modalities could improve overall detection capabilities.

While reading related articles, it was observed that the recent advancements in ML and DL techniques, such as Convolutional Neural Networks (CNNs) and Long Short-Term Memory (LSTM) networks, have significantly enhanced the accuracy of ECG analysis, achieving impressive results in arrhythmia detection [19]. Moreover, innovative approaches like disease-specific attention mechanisms and multi-view adaptive networks have improved model interpretability and performance, making ECG a reliable tool for clinicians [20], [21]. The integration of ML with traditional ECG analysis addresses challenges like individual physiological differences, further solidifying ECG's role in arrhythmia detection [21], [22].

In terms of accuracy, various ML methods have also shown promising results in HD detection, with Random Forest achieving an accuracy of 0.929, outperforming Support Vector Machine and Logistic Regression models [23]. Additionally, DL models, particularly the GAN-LSTM ensemble, have demonstrated high accuracy and F1-scores in ECG analysis, indicating their effectiveness in handling imbalanced data [14], [24]. However, CNNs not only offer significant advantages in ECG signal processing, including high accuracy in diagnosing various cardiac conditions, as demonstrated by their performance in interpreting 12-lead ECGs, where they achieved an area under the curve (AUC) of at least 0.960 for 84.2% of diagnostic classes [25]. But, CNNs can also effectively segment ECG waveforms, enhancing the analysis and diagnosis process [26]. However, limitations exist, such as challenges related to interpretability and the need for large, well-annotated datasets for training [27]. While CNNs outperform traditional methods, they may still struggle with specific conditions, as seen in their comparative performance against cardiologists for certain diagnoses [25]. Furthermore, the presence of noise in ECG signals can hinder the effectiveness of CNNs, necessitating advanced denoising techniques to improve signal quality before analysis [28]. Thus, while CNNs present promising advancements, addressing these limitations is crucial for their broader clinical application.

The accuracy of DL techniques for HD detection varies significantly across different methodologies. For instance, a hybrid deep neural network model that combines convolutional and recurrent neural networks achieved superior accuracy by analyzing audio recordings of heartbeats, outperforming existing methods [29]. In another study, convolutional neural networks (CNNs) applied to ECG signals demonstrated an average classification accuracy of approximately 93%, with post-processing filters enhancing this to nearly 100% [30]. Additionally, a review of DL neural networks highlighted the importance of feature extraction and selection, which are critical for improving diagnostic accuracy [14]. Furthermore, DL techniques applied to medical imaging, such as echocardiograms, have shown promise in detecting subtle abnormalities, thus enhancing early detection capabilities [31]. Overall, while various DL approaches show high accuracy, the specific techniques and data utilized play a crucial role in their effectiveness [32].

As the development of DL models consists of mainly two stages, extraction of features from raw input data and training of the model, the feature extraction techniques for raw input data in DL are crucial for enhancing classification and detection accuracy, with various methods offering unique advantages to ECG signal analysis [33]. One common approach is time domain analysis, which involves extracting features directly from the time series data of ECG signals, focusing on metrics such as heart rate variability and R-R intervals. Another technique is frequency domain analysis, where methods like Fast Fourier Transform (FFT) are used to analyze the frequency components of ECG signals, aiding in the identification of arrhythmias. The wavelet transform, specifically the Discrete Wavelet Transform (DWT), is employed to decompose ECG signals into different frequency components, which effectively removes noise and enhances feature extraction for classification tasks. In recent years, DL models such as hybrid architectures like CNN-LSTM and attention-based transformers have been used to automatically extract features from raw ECG data, achieving high classification accuracy [34]. While these techniques significantly improve ECG analysis, challenges remain in standardizing methods across diverse datasets and ensuring robustness against noise and variability in signal quality.

While studying related articles for the classification of HD using images, it was observed that CXR datasets used for pneumonia detection can be effectively utilized for HD diagnosis and classification. The methodologies used in DL for CXR analysis demonstrate that these images can be adapted for various conditions, including HD. For instance, studies have shown that CNNs can classify multiple diseases from CXR images, achieving high diagnostic accuracy for both lung and heart conditions [35], [36]. Moreover, the use of transfer learning and ensemble methods has proven beneficial in enhancing classification performance across different diseases, including pneumonia and HD [36], [37]. The versatility of CXR images, combined with advanced ML techniques, allows for the identification of various pathologies, making them a valuable resource for diagnosing HD alongside pneumonia [37]. Thus, leveraging existing

pneumonia datasets can facilitate improved HD detection and classification.

Recently, several researchers have proposed lightweight convolution methods that aim to improve the efficiency of DL models significantly so that they can be employed in resource constrained environments. Both 1-D CNNs and 2-D CNNs show promise in processing sequential data, such as time series data, signal processing and images respectively. For instance, [38] introduced 1-D SKCNN, which uses a selective Kernel/filter to perform intra-pulse modulation classification of radar signals. The proposed model adjusts the receptive field adaptively using a selective kernel mechanism which removes the need for time-frequency transformations and thus, reduces pre-processing time. However, the 1-D SKCNN is sensitive to class order during training time, which can sometimes affect it's performance. The authors tried to address this issue by adding convolutional classification layer without weight-sharing which improved accuracy. Reference [39] developed a 1-D Convolutional Augmented Transformer for hyperspectral image classification, which combines transformers with 1-D convolutions to handle redundancy of spectral features and limited labeled data. Though these proposed methods show promising results in sequential data, their ability to capture spatial features in images remain limited.

For 2-D convolutions, a novel model called ChannelNets by [40] shows a significant leap in lightweight CNN architectures. The proposed methodology by the authors employs channel-wise convolutions to replace dense connections among feature maps, which reduces parameters and computational costs while also retaining adequately high accuracy. The proposed model uses group channel-wise convolutions to address information inconsistency caused by grouping and depth-wise separable channel-wise convolutions to further compress the network. Notably, the reduction of the FC layer with c convolutional classification layer is ChannelNets drastically reduces parameters in the final layer. However, this layer assumes adjacent features to have equal importance for adjacent classes, which may not always hold true in real world applications. Here, to mitigate this, the authors proposed a convolutional classification layer without weight-sharing, enhancing performance and robustness. Other lightweight architectures, such as MobileNets and ShuffleNets, also leverage depth-wise separable and group convolutions but often require deeper architectures to maintain performance, offsetting some efficiency gains.

Despite these advancements, challenges still remain. Lightweight models often struggle with tasks requiring fine-grained spatial information, such as in case of disease classification tasks. Additionally, integrating these models into multimodal diagnostic systems, which combine data from images, text, and sensors, remains an open problem. Future researchers could also explore hybrid models that leverage the strengths of both 1-D and 2-D convolutions, along with attention mechanisms, to achieve more robust and accurate multimodal diagnostics. Addressing these challenges will be crucial for deploying lightweight models in resource-constrained environments, particularly in fields like healthcare.

III. RESEARCH SCOPE, CONTRIBUTIONS, AND PAPER OUTLINE

A. RESEARCH GAP

Literature review reveals that, while DL methods, such as CNN, have revolutionized ECG and CXR analysis for cardiovascular diagnostics, their computational demands remain a significant challenge. Traditional feature extraction techniques, such as time-domain, frequency-domain, and wavelet transformations, while effective, require substantial processing power and time. This limits their feasibility in low-resource settings, where rapid diagnostic response is critical.

The diagnostic accuracy of CNNs is high (AUC > 0.960 for multiple classes in ECG data) [25] and frequently outperform conventional techniques [15], they are impeded by the lengthy training and inference periods caused by the repetitive computations that are a part of standard convolutions [26]. Particularly in areas with limited resources, this computational load limits their use in real-time clinical applications [9]. Although recent advancements such as multi-view networks and attention mechanisms have enhanced CNN's interpretability and adaptability, the core convolutional inefficiencies still exist [20].

B. MOTIVATION OF RESEARCH

Keeping the Research gap in mind, this study identifies the need for a more efficient convolution technique that maintains DL Algorithm's diagnostic accuracy while significantly reducing computational time and resource requirements for series of Convolution operations. The integration of the WT-based Circular Convolution method offers a promising solution by decreasing the number of required arithmetic operations, enhancing processing speed without sacrificing performance for both ECG Signals and CXR Images. This approach aims to make extraction of features and classification of HD for cardiovascular diagnostics more practical for clinical use, especially in time-sensitive, resource-constrained settings.

C. OBJECTIVE OF RESEARCH

Based on the identified research gap and motivation, the objectives of this study have been systematically addressed as follows:

1. Collection and analysis of standard 1-D ECG datasets, including the MIT-BIH and PTB-XL datasets, along with a comprehensive dataset containing labeled Optical Coherence Tomography (OCT) and CXR images for the 2-D CXR dataset.

2. Data preprocessing to ensure quality and uniformity across both 1-D and 2-D datasets.

3. Extraction of key features from 1-D ECG signals and 2-D CXR images, applied for single- and multi-stage processing.

4. Selection of classifiers for analysis, including ANN, LSTM, RNN, GRU, DT, RF, SVM, LR, and NB.

5. These classifiers have been chosen because they have exhibited effective and consistent performance across a range of problems.

6. Training and testing of the proposed model to evaluate its accuracy and robustness.

7. Comprehensive assessment of the model's performance using relevant metrics.

8. Ranking of the proposed model based on feature extraction time and additional performance metrics to assess its efficiency.

9. Outlining the primary contributions and significance of this work in advancing efficient diagnostic methods for cardiovascular applications.

D. ORGANIZATION OF THE PAPER

Section I introduces the study, highlighting the importance of efficient feature extraction in cardiovascular diagnostics. Section II reviews existing literature, while Section III outlines the research gap, motivation, objectives, and paper structure. Section IV details the ECG and CXR datasets used. Section V describes the feature extraction processes for 1-D ECG signals and 2-D CXR images.

Section VI compares computational requirements of various convolution methods, and Section VII presents the development of detection models based on the extracted features. Section VIII covers the simulation experiments, and Section IX ranks the models by efficiency and accuracy. Section X and XI illustrate the mathematical methodologies for 1-D and 2-D convolution, respectively. Section 12 concludes the paper, summarizing contributions and future research directions.

IV. DATASETS

A. 1-D ECG SIGNAL DATASETS

1) MIT-BIH DATASET

The MIT-BIH Dataset, developed by the Massachusetts Institute of Technology (MIT) in collaboration with Beth Israel Hospital (BIH) contains 48 ECG recordings, each lasting approximately 30 minutes and sampled at a frequency of 360 Hz. The recordings primarily utilize lead II, which effectively captures the electrical activity of the heart. Each ECG recording is accompanied by target files that provide classifications for various heartbeat types, including normal (N), atrial premature beats (A), and premature ventricular contractions (V), among others (N, S, V, F, Q). For the purpose of this study, 12,000 ECG Signals were chosen at random from the MIT-BIH's collection of 1,09,446 Signals. These signals were selected in a balanced proportion of HD and Non HD Classes for binary classification. The link for the aforementioned dataset is *MIT-BIH Arrhythmia Database*

TABLE 1. Feature extraction stages and corresponding number of samples per ECG signal.

Stages of Feature Extraction	Number of Samples in 1 ECG Signal
0 (Raw ECG)	189
1	63
2	21
3	7

2) PTB-XL DATASET

The PTB-XL dataset, developed by the Physikalisch-Technische Bundesanstalt (PTB), contains 21,837 clinical 12-lead ECG recordings, each lasting between 10 to 60 seconds and sampled at 500 Hz and 100 Hz. These recordings capture the electrical activity of the heart from multiple perspectives. Each ECG record includes detailed annotations that identify various cardiac abnormalities, such as myocardial infarction and bundle branch blocks, among other HD. The dataset also categorizes information into diagnostic, form, and rhythm classes, offering a valuable resource for developing and evaluating models for arrhythmia detection and other cardiac diagnoses. Furthermore, just as previously mentioned, 12,000 balanced class ECG Samples were selected from PTB Dataset for binary classification. The dataset can be found at *PTB-XL, a large publicly available electrocardiography dataset*

B. 2-D CHEST X-RAY IMAGE DATASET

1) LARGE DATASET OF LABELED OPTICAL COHERENCE TOMOGRAPHY (OCT) AND CHEST X-RAY IMAGES

The Large Dataset of Labeled Optical Coherence Tomography (OCT) and Chest X-Ray Images contains 5,863 labeled CXR images categorized as normal or pneumonia, which are crucial for detecting respiratory complications in HD patients. CXR are employed in studies to identify cardiothoracic abnormalities such as cardiomegaly (a disease where the size of heart gets larger than normal) and pulmonary edema (a condition where excess fluid builds up in the lungs, making it hard to breathe), both of which are linked to heart failure. Additionally, these images help predict cardiovascular events by assessing lung conditions, often used alongside ECG data in multimodal models. The dataset also aids in transfer learning, with models pretrained on X-ray images being adapted for heart-specific tasks, contributing to the development of robust diagnostic tools for cardiovascular and respiratory health. The dataset was accessed from *Large Dataset of Labeled Optical Coherence Tomography (OCT) and Chest X-Ray Images*

It was observed that the dataset has imbalance between the classes Pneumonia and Healthy (60-40)

V. FEATURES EXTRACTION USING DIFFERENT 1-D AND 2-D CIRCULAR CONVOLUTION METHODS

In this study, a low-pass filter [0.25, 0.50, 0.25] was selected for the convolution of one-dimensional (1-D) ECG signals.

This choice was informed by an extensive review of relevant literature, where this filter configuration demonstrated a consistent balance between noise reduction and signal fidelity. Its design effectively attenuates high-frequency noise while preserving the primary signal components, making it suitable for ECG signal processing in accordance with prior works.

For two-dimensional (2-D) image convolution, a filter matrix defined as:

$$\begin{bmatrix} \frac{1}{16} & \frac{2}{16} & \frac{1}{16} \\ \frac{2}{16} & \frac{4}{16} & \frac{2}{16} \\ \frac{1}{16} & \frac{2}{16} & \frac{1}{16} \end{bmatrix}$$

was chosen after evaluating the performance of over 15 different filter configurations. This filter provided an optimal compromise between smoothing and edge preservation, effectively reducing image noise while maintaining key structural details. The empirical testing confirmed its suitability for the image processing tasks specific to this experiment.

A. 1-D CONVOLUTION BASED EXTRACTION OF FEATURES FROM ECG SIGNALS USING THREE DIFFERENT METHODS

An ECG signal, consisting of 189 samples, was processed using two different low-pass filters, one with a size of 3 and the other with a size of 5. The convolution of the signal with each filter was carried out using three distinct methods: Time Domain Circular Convolution, Circular Convolution via the DFT, and the WT. After each convolution, the filter was shifted along the signal in a non-overlapping manner, and the process was repeated across the entire signal length. Following this, average pooling was applied to reduce the dimensionality of the convoluted signal. This completed one stage of the feature extraction process. The features extracted from the three methods are same, but the WT method proved to be significantly faster and it's computational efficiency is discussed in detail in Section V. In Table 1, the effect on the number of samples with the increase in stages is described in detail. Furthermore, Fig 1 illustrates how the three different Convolution operations are employed for extraction of features from raw ECG signals in this study.

The three different convolution techniques are explained in detail in the sections ahead.

1) TIME DOMAIN CIRCULAR CONVOLUTION (TDCC)

TDCC is achieved by performing the convolution directly between two sequences of finite length, considering the sequences to be periodic. In TDCC, each output element is computed by summing the product of the circularly shifted input sequence and the filter sequence. This method is effective in handling situations where the signal is believed to be cyclical or repetitive in nature. The equation to calculate the circular convolution in the time domain between two sequences $s[n]$ (input signal) and $h[n]$ (filter), both of length N, is as follows:

$$y[n] = \sum_{m=0}^{N-1} s[m] \cdot k[(n-m) \bmod N] \tag{1}$$

Here, $y[n]$ represents the resulting sequence after applying the convolution, and the modulo operation ensures that the indices wrap around, treating the sequence as periodic. For ECG signals, this operation captures cyclical patterns such as repetitive heartbeats, allowing the model to retain essential periodic features while reducing computational complexity compared to linear convolution. The real time implementation and it's calculation is illustrated in Appendix A-A

2) DISCRETE FOURIER TRANSFORM DOMAIN CIRCULAR CONVOLUTION (DFTCC)

DFTCC is a method of computing the convolution of two finite-length sequences using the DFT. According to the convolution theorem, convolution in the time domain corresponds to multiplication in the frequency domain, making DFT an efficient tool for this purpose. When sequences are transformed into the frequency domain via DFT, the convolution process becomes a simple pointwise multiplication of their DFT coefficients. After this multiplication, an Inverse DFT (IDFT) operation is applied to the resultant sequence, to transform it back into the time domain, yielding the circular convolution output. Steps to perform circular convolution using DFT method are as follows.

a: STEP 1: COMPUTE DFT OF THE INPUT SEQUENCES

Let $s[n]$ be the input sequence and $h[n]$ be the filter sequence. First, calculate the DFT of both sequences:

$$S[k] = \sum_{n=0}^{N-1} s[n] \cdot e^{-j \cdot 2\pi \cdot \frac{k \cdot n}{N}} \tag{2}$$

$$H[k] = \sum_{n=0}^{N-1} h[n] \cdot e^{-j \cdot 2\pi \cdot \frac{k \cdot n}{N}} \tag{3}$$

Here, $S[k]$ and $H[k]$ represent the DFTs of $s[n]$ and $h[n]$, respectively, and N is the length of the sequences.

b: STEP 2: PERFORM ELEMENT-WISE MULTIPLICATION IN THE FREQUENCY DOMAIN

Now, perform pointwise multiplication in the frequency domain as follows:

$$Y[k] = S[k] \cdot H[k] \tag{4}$$

where $Y[k]$ is the DFT of the output sequence $y[n]$.

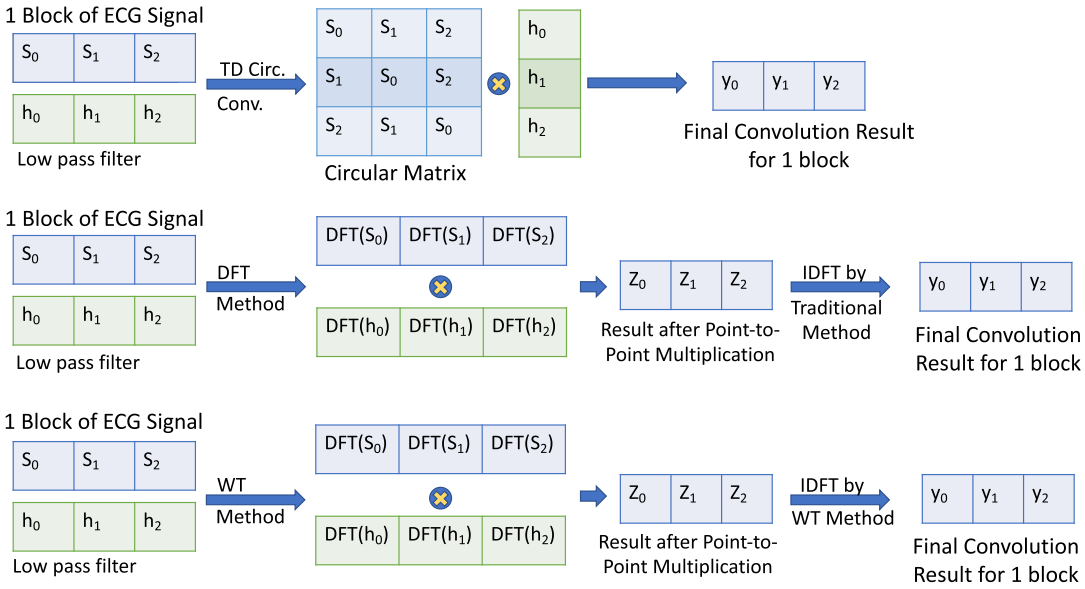

FIGURE 1. Implementation of circular convolution using TD, DFT, WT methods on one ECG block.

c: STEP 3: COMPUTE THE INVERSE DFT TO OBTAIN CIRCULAR CONVOLUTION OUTPUT

To obtain the result of the circular convolution in the time domain, calculate the Inverse DFT (IDFT) of $Y[k]$:

$$y[n] = \frac{1}{N} \sum_{k=0}^{N-1} Y[k] \cdot e^{j \cdot 2\pi \cdot \frac{k \cdot n}{N}} \tag{5}$$

The sequence $y[n]$ is the result of the circular convolution between $s[n]$ and $h[n]$.

d: SUMMARY OF STEPS

1. Calculate the DFT of the input sequence $s[n]$ and the filter sequence $h[n]$. 2. Perform element-wise multiplication in the frequency domain to get $Y[k] = S[k] \cdot H[k]$. 3. Apply the inverse DFT on $Y[k]$ to obtain the circular convolution result $y[n]$.

The calculation for an example of DFT based Circular Convolution for a 3-point signal and kernel is illustrated in Appendix X.B.

3) WINOGRAD TRANSFORM CIRCULAR CONVOLUTION (WTCC)

The WT is a technique used to compute the DFT in an optimized way, especially for small input sizes. It belongs to a class of algorithms that aim to reduce the computational complexity of the DFT by minimizing the number of arithmetic operations. Unlike the Fast Fourier Transform (FFT), which scales more efficiently for large input sizes, Winograd's approach is particularly useful for small-length DFTs and can significantly reduce the number of multiplications needed.

As the primary goal of the Winograd method is to reduce the number of expensive arithmetic operations, especially multiplications, in the DFT computation, the DFT of a sequence can be computed using WT Method by using only 20% of the multiplications required by Standard DFT Method. Multiplications are typically more computationally intensive than additions, so minimizing them can lead to more efficient algorithms, especially in real-time scenarios, such as Circular Convolution discussed in the proposed study. Even though the algorithm is more complex to implement than other methods used in this study, it's advantages are far more rewarding in terms of less computational efforts.

The WT works for many signal lengths. The proposed study employed 3-Point and 5-Point Winograd for 1-D and 3-Point Winograd for 2-D.

a: WINOGRAD DFT FORMULA

For a sequence $\mathbf{s} = [s[0], s[1], s[2]]$, the 3-point DFT using Winograd's method is calculated as follows:

1. Compute intermediate values:

$$t_1 = s[1] + s[2] \tag{6}$$
$$m_0 = s[0] + t_1 \tag{7}$$
$$m_1 = (\cos\left(\frac{2\pi}{3}\right) - 1) \cdot t_1 \tag{8}$$
$$m_2 = j \cdot \sin\left(\frac{2\pi}{3}\right) \cdot (s[1] - s[2]) \tag{9}$$

2. Calculate the DFT outputs:

$$S[0] = m_0 \tag{10}$$
$$S[1] = m_0 + m_1 + m_2 \tag{11}$$

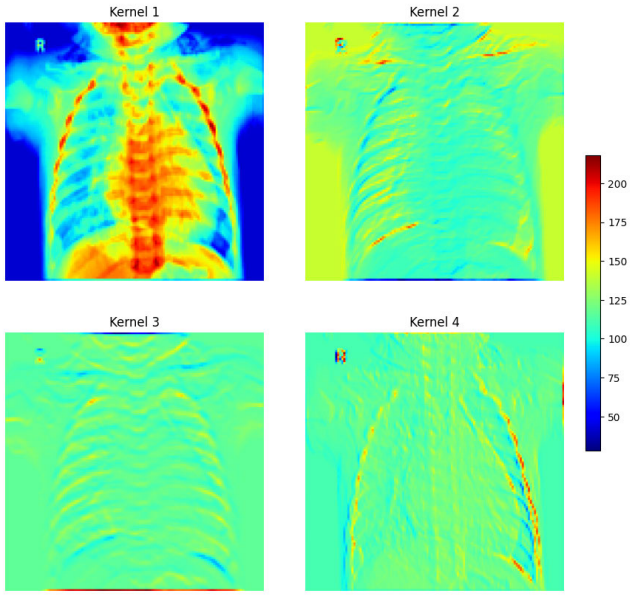

FIGURE 2. Heatmaps of extracted features using different kernels.

$$S[2] = m_0 + m_1 - m_2 \tag{12}$$

where j is the imaginary unit, with constants $\cos\left(\frac{2\pi}{3}\right) = -0.5$ and $\sin\left(\frac{2\pi}{3}\right) = 0.866$.

Note: When calculating the DFT inverse using the Winograd Transform:

$$S[0] = m_0 \tag{13}$$
$$S[1] = m_0 + m_1 - m_2 \tag{14}$$
$$S[2] = m_0 + m_1 + m_2 \tag{15}$$

and the results have to be normalized.

Calculations for Winograd-based circular convolution are illustrated with an example in Appendix X.C.

B. 2-D CONVOLUTION BASED EXTRACTION OF FEATURES FROM CXR IMAGES USING THREE DIFFERENT METHODS

To evaluate the robustness and efficiency of the WT method in circular convolution, the current study extends circular convolution to images using three approaches: TD, DFT, and WT, providing a comprehensive analysis. CXR images were convolved with a fixed 3×3 kernel across the three methods, followed by max-pooling, conducted through one, two, and three stages of convolution and pooling.

Use of Non-Overlapping static Filters: For this study, as with the ECG signals, *non-overlapping filters* (with stride 3×3) were applied to the images. This approach ensures each filter operates independently on distinct image regions, avoiding overlap and redundancy in the convolution process, so each area of the image is convolved with its filter precisely once.

Figure 3 demonstrates the application of circular convolution on a single convolution block of an image, for the various methods employed in this study. Several static filters were employed and tested for performing circular convolution on the images as shown in Figure 2 where Kernel 1 is a low pass filter used in the proposed manuscript and explained in Section V. Kernel 2 is a large Gaussian blur kernel of size 5×5. Kernel 3 is a Laplacian kernel, and kernel 4 is a high-pass kernel. All of the heatmaps of the aforementioned features were plotted after several stages of convolution in order to show the features extracted from various kernels using the WT-based circular convolution. However, in the proposed study, the features generated from the low pass filter (kernel 1) were employed for training the models as it proved to be more robust for maintaining high accuracy of the models.

1) 2-D TIME DOMAIN CIRCULAR CONVOLUTION (2D-TDCC)

In the proposed study, 2-D Circular Convolution is applied in the time domain, an important operation in image processing for filtering or transforming images while maintaining their original dimensionality. This method assumes periodic boundary conditions for the image, meaning that when the filter extends beyond the boundaries, the values wrap around to the opposite side of the image. This characteristic ensures that the convolution result retains the same dimensions as the input.

Mathematical Formulation of 2-D Circular Convolution: For two discrete 2-D signals, an image $I[m, n]$ of size $M \times N$ and a filter $h[m, n]$ of size $P \times Q$, the circular convolution $C[m, n]$ is expressed as follows:

$$C[m, n] = \sum_{p=0}^{P-1} \sum_{q=0}^{Q-1} I((m-p) mod M, (n-q) mod N) \cdot h[p, q] \tag{16}$$

In this formula, the modulo operation ensures that the convolution is circular, such that when the indices exceed the dimensions of the image M and N, they wrap around to remain within bounds.

Circular Matrix Formation: In this study, the input image is transformed into a *block circulant matrix*, which allows for an efficient representation of the convolution. The block circulant matrix is formed by circularly shifting each row of the image:

- The first row corresponds to the original image.
- The subsequent rows are obtained by shifting the pixels of the image to the right, with wrap-around from the last to the first position.

This transformation yields a circulant matrix C, where each row is a shifted version of the image:

$$C = \begin{bmatrix} I[0] & I[N-1] & \cdots & I[1] \\ I[1] & I[0] & \cdots & I[2] \\ \vdots & \vdots & \ddots & \vdots \\ I[N-1] & I[N-2] & \cdots & I[0] \end{bmatrix}$$

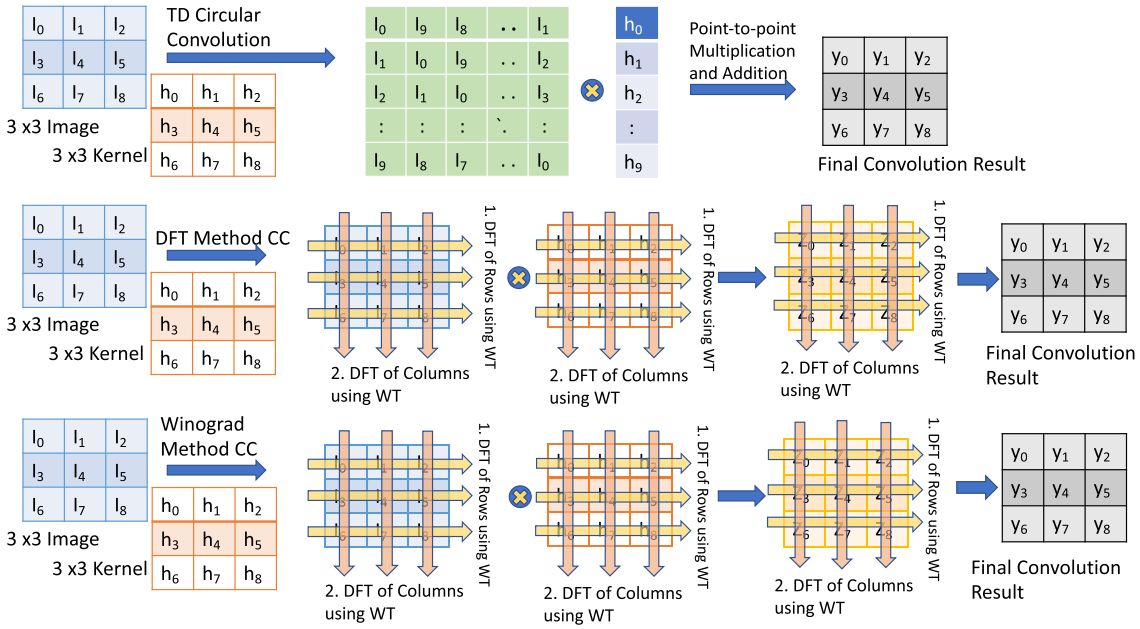

FIGURE 3. Implementation of circular convolution using TD, DFT, WT methods on a 3 × 3 Image with 3 × 3 kernel.

The block circulant structure of this matrix ensures the periodic boundary condition for the circular convolution, a key aspect of the proposed method.

Point-to-Point Multiplication: In the proposed approach, the convolution operation is performed by element-wise multiplication between the circular matrix C and the filter h. For each position (m, n) in the image, the corresponding circularly shifted version of the image is aligned with the filter. The convolution result is computed as the sum of point-wise multiplications between the image values and the filter values:

$$C[m,n] = \sum_{p=0}^{P-1}\sum_{q=0}^{Q-1} C_{m-p,n-q} \cdot h[p,q] \tag{17}$$

This operation ensures that each pixel in the output image is influenced by the neighborhood of pixels in the input image, in accordance with the filter. The periodic nature of the circular convolution is captured by the structure of the circular matrix. For the example illustration, refer to section XI.A.

2) 2-D DISCRETE FOURIER TRANSFORM DOMAIN CIRCULAR CONVOLUTION (2-D DFTCC)

2-D Circular Convolution is also performed using the DFT method, which leverages the efficiency of frequency domain operations. The DFT-based approach is generally advantageous for larger filters or images, as it reduces the computational burden of direct convolution. However, when applied to smaller filters, such as in the present case with a 3-point filter, the additional overhead of transforming the image and filter between the spatial and frequency domains using the traditional DFT method can outweigh the benefits, leading to slower performance compared to the time-domain method.

Mathematical Formulation Using DFT: The convolution theorem states that circular convolution in the time domain corresponds to element-wise multiplication in the frequency domain. For two 2-D discrete signals, an image $I[m, n]$ and a filter $h[m, n]$, their 2-D circular convolution can be computed efficiently by the following steps:

1) *Compute the 2-D DFT of the image and the filter:* First, the image and the filter are transformed from the spatial domain to the frequency domain using the 2-D DFT. The DFT for a 2-D image of size $M \times N$ is given by:

$$F[k_1,k_2] = \sum_{m=0}^{M-1}\sum_{n=0}^{N-1} I[m,n] e^{-2\pi j\left(\frac{k_1 m}{M}+\frac{k_2 n}{N}\right)} \tag{18}$$

where $F[k_1, k_2]$ is the DFT of the image, and k_1 and k_2 are the frequency domain indices. A similar transform is applied to the filter $h[m, n]$, yielding the filter's DFT.

2) *Element-wise Multiplication in the Frequency Domain:* Once both the image and the filter are transformed into the frequency domain, circular convolution is performed by element-wise multiplication of their respective DFTs:

$$G[k_1,k_2] = F[k_1,k_2] \cdot H[k_1,k_2] \tag{19}$$

where $G[k_1, k_2]$ is the product of the DFTs of the image and filter in the frequency domain.

3) *Inverse 2-D DFT to Obtain the Convolution Result:* The final step involves transforming the product $G[k_1, k_2]$

back to the spatial domain using the inverse 2-D DFT (IDFT):

$$I'[m,n] = \frac{1}{MN}\sum_{k_1=0}^{M-1}\sum_{k_2=0}^{N-1} G[k_1,k_2]e^{2\pi j\left(\frac{k_1 m}{M}+\frac{k_2 n}{N}\right)} \tag{20}$$

This results in the circularly convolved image $I'[m,n]$, where m and n are the spatial indices of the output image.

Point-to-Point Multiplications in the Frequency Domain: The multiplication step is performed element-wise between the DFTs of the image and the filter. This step is highly efficient because each element of the transformed image interacts with the corresponding element of the transformed filter. However, in the case of smaller filters, the benefit of this efficiency can be diminished by the overhead of the transformations. It's example is formulated and calculated in Section XI.B.

3) WINOGRAD DOMAIN CIRCULAR CONVOLUTION (WDCC)

Just as in 1-D, in 2-D, Circular Convolution is also implemented using the Winograd-based DFT approach. Winograd's algorithm is designed to minimize the number of multiplications required in convolution operations, which leads to significant performance gains, particularly for small filters, as discussed earlier in 1-D. This method proves to be faster than both the traditional DFT method and the time-domain convolution, primarily due to its optimized use of arithmetic operations and significant reduction in multiplication operations.

Mathematical Formulation Using Winograd's Algorithm: The Winograd algorithm exploits the structure of small-length DFTs to reduce computational complexity. Specifically, for a 3-point filter, the 1-D DFT and inverse DFT can be computed with fewer arithmetic operations than conventional FFT methods. The following outlines the steps for performing 2-D Circular Convolution using Winograd's DFT:

1) *Winograd DFT of the Image and Filter:* The 1-D DFT for each row of the image $I[m,n]$ and the filter $h[m,n]$ is computed using Winograd's algorithm. For a 3-point DFT, the transformation is computed as follows:

$$WDFT(x) = [m_0, m_1, m_2] \tag{21}$$

where m_0, m_1, and m_2 are the transformed coefficients based on the sum of weighted input values, as defined by the Winograd equations. After processing rows, the same operation is applied to the columns of the intermediate matrix, yielding the full 2-D Winograd DFT of the image and the filter.

2) *Element-wise Multiplication in the Frequency Domain:* Once the 2-D Winograd DFT is obtained for both the image and the filter, circular convolution is performed by element-wise multiplication in the frequency domain:

$$G[k_1,k_2] = WDFT(I[m,n]) \cdot WDFT(h[m,n]) \tag{22}$$

where $G[k_1,k_2]$ represents the product of the DFTs of the image and the filter in the frequency domain.

3) *Inverse Winograd DFT:* The final step is to transform the result back into the spatial domain using the inverse Winograd DFT (IDFT), which again applies Winograd's optimized operations to each row and column:

$$I'[m,n] = WIDFT(G[k_1,k_2]) \tag{23}$$

This yields the circularly convolved image $I'[m,n]$.

C. PERFORMANCE IMPROVEMENT AND COMPUTATIONAL EFFICIENCY

The Winograd-based method significantly reduces the number of arithmetic operations compared to both the DFT and time-domain methods. For the 3-point DFT, this reduction translates into a much faster execution time, particularly when the image is processed in blocks. Unlike the traditional DFT, Winograd's approach minimizes unnecessary operations and optimizes the DFT computation for small filter sizes. As a result, in the present case, the Winograd method outperforms both the DFT and time-domain methods significantly. The application of WT-based circular convolution is illustrated in Appendix B-C.

VI. COMPARISON OF COMPUTATIONAL EFFORTS OF DIFFERENT METHODS

A. CPU TIME

The CPU time measurements in this study were carried out on a laptop featuring an Apple M1 processor and 8 GB of RAM. This configuration, with the M1's ARM-based architecture, was chosen to balance performance and energy efficiency for computational tasks. The reported CPU times therefore reflect the processing capabilities of this setup, offering a standard reference point for this study.

1) 1-D

The computational efforts are depicted for a single convolution block, one ECG signal, and the total feature extraction time for 12,000 ECG signals, which involves three stages of convolutions followed by pooling, as shown in Table 2. The WT method proved to be significantly faster for feature extraction from raw ECG signals compared to the TD and DFT methods. The proposed method is approximately 2.86 times faster than the TD method and 4.73 times faster than the DFT method for three stages of convolution and pooling. As the number of stages increases, the time savings achieved by using the WT method would become even more substantial, reducing model development time, conserving computational resources, and accelerating the training time for DL models.

2) 2-D

The computational efforts required for feature extraction using a single convolution operation (3×3), a single CXR

TABLE 2. CPU time and relative speed comparison for 1-D circular convolution.

Filter Size	Metric	Time Domain		DFT		Winograd (WT)	
		Time (s)	Relative Speed	Time (s)	Relative Speed	Time (s)	Baseline (1.00)
3-Point	Single Sequence (10^{-5})	1.39	1.14× slower	5.61	4.60× slower	**1.22**	**Fastest**
	Single ECG (10^{-4})	2.66	1.49× slower	10.37	5.79× slower	**1.79**	**Fastest**
	12k MIT-BIH (s)	5.35	2.86× slower	8.84	4.73× slower	**1.87**	**Fastest**
5-Point	Single Sequence (10^{-5})	1.98	1.17× slower	8.13	4.81× slower	**1.69**	**Fastest**
	Single ECG (10^{-4})	5.49	2.63× slower	13.66	6.54× slower	**2.09**	**Fastest**
	12k MIT-BIH (s)	6.45	3.24× slower	10.93	5.49× slower	**1.99**	**Fastest**

Times are provided in seconds (s) for various dataset sizes. Multipliers indicate 10^{-5} or 10^{-4} for scaled times. Winograd consistently shows the fastest performance across configurations.

TABLE 3. Performance comparison for feature extraction on 2-D images with 3 × 3 kernel.

Method	3x3 Image		256x256 Image	
	Time (s)	Ratio	Time (s)	Ratio
WT (proposed)	0.99×10^{-4}	1	0.84	1
TD	1.91×10^{-4}	1.92	1.70	2.02
DFT	3.26×10^{-4}	3.29	2.19	2.60

image (256×256), and a set of 5,865 CXR images (256×256) with a 3 × 3 filter are depicted in Table 3 and 4. Additionally, Table 4 presents the complete model development time for HD classification using CXRCXR images by applying the three feature extraction methods investigated in this study.

As shown in Table 4, using the WT method for faster, accelerated feature extraction significantly reduced model development time. The WT method was observed to be approximately 4.50 times faster than TD-CNN and 4.04 times faster than DFT-CNN. Similar trends were observed across other DL models, namely CLSTM, CRNN, and CGRU, where the prefix "C" in each model denotes the use of a Convolutional layer for feature extraction, as applied in this study.

VII. DEVELOPMENT OF DETECTION MODELS USING EXTRACTED FEATURES

In the proposed study, relatively simple and standard models were selected to classify the extracted features from ECG signals and CXR images. These models were chosen for their consistent and effective performance across diverse problem domains, making them well-suited for this classification task. To ensure a fair comparison, the DL models—including Neural Networks, LSTM, RNN, and GRU—were configured with a consistent architecture: two hidden layers containing 128 and 64 neurons, respectively, with 20% dropout between the two layers and an output layer with a sigmoid activation function for binary classification. Figure 4 illustrates the structure of the complete DL classification models [41]. Traditional ML models, such DT, RF, SVM, LR, NB, were also employed [42]. Each model's performance was evaluated, allowing for a comparative ranking based on accuracy, computational efficiency, and robustness in feature classification for ECG and CXR datasets. This approach aims to identify the most suitable model configurations for cardiovascular diagnostics in a clinical context.

VIII. SIMULATION BASED EXPERIMENTS ON THE DEVELOPED MODELS

A. 1-D MODEL

The model development is shown in Figure 5 in this study, classification was performed for both stage extracted features, 2-Stage and 3-Stage as shown in the figure, to observe the effect of the number of layers.

B. 2-D MODEL

The model development is illustrated in Figure 6. Since feature extraction was already performed on the data, only a few layers were required in the DL models for accurate classification of the images. Using additional layers would increase complexity without substantial benefits, as the essential features had already been isolated in preprocessing. By limiting the model depth, we focused on efficient learning from the extracted features, reducing both computational demands and potential overfitting. This streamlined approach allows the model to leverage the existing features effectively without unnecessary depth.

IX. RANKING OF MODELS

To determine the optimal model for HD classification, we evaluated various ML and DL models based on three key performance metrics: accuracy, F1 score, and Area Under the Curve (AUC) values. These metrics offer a comprehensive view of each model's effectiveness, considering both precision and recall (through the F1 score), overall predictive accuracy, and the model's ability to discriminate between positive and negative cases (AUC) [43]. To systematically rank the models, two multi-criteria decision-making algorithms were employed: the Technique for Order of Preference by Similarity to Ideal Solution (TOPSIS) and Multiple Regression Analysis (MRA). Each algorithm applies a unique approach to aggregate the performance metrics and produce a ranked list, allowing for a more informed selection of the best-performing model.

TABLE 4. Comparison of model-development times for different DL models.

Model	Features Extraction Method	Features Extraction Time(s)	Training Time (s)	Total Time (s)	Ratio w.r.t WT
CNN	WT (Proposed)	12,516	715.59	13,231.60	1
	TD	58,739	715.59	59,454.60	4.50
	DFT	52,840	715.59	53,555.60	4.04
CRNN	WT (Proposed)	12,516	1509.82	14,025.82	1
	TD	58,739	1509.82	60,248.82	4.30
	DFT	52,840	1509.82	54,349.82	3.87
CGRU	WT (Proposed)	12,516	4155.30	16,671.30	1
	TD	58,739	4155.30	62,849.30	3.77
	DFT	52,840	4155.30	56,995.30	3.41
CLSTM	WT (Proposed)	12,516	5,509.82	18,025.82	1
	TD	58,739	5,509.82	64,248.82	3.56
	DFT	52,840	5,509.82	58,349.82	3.23

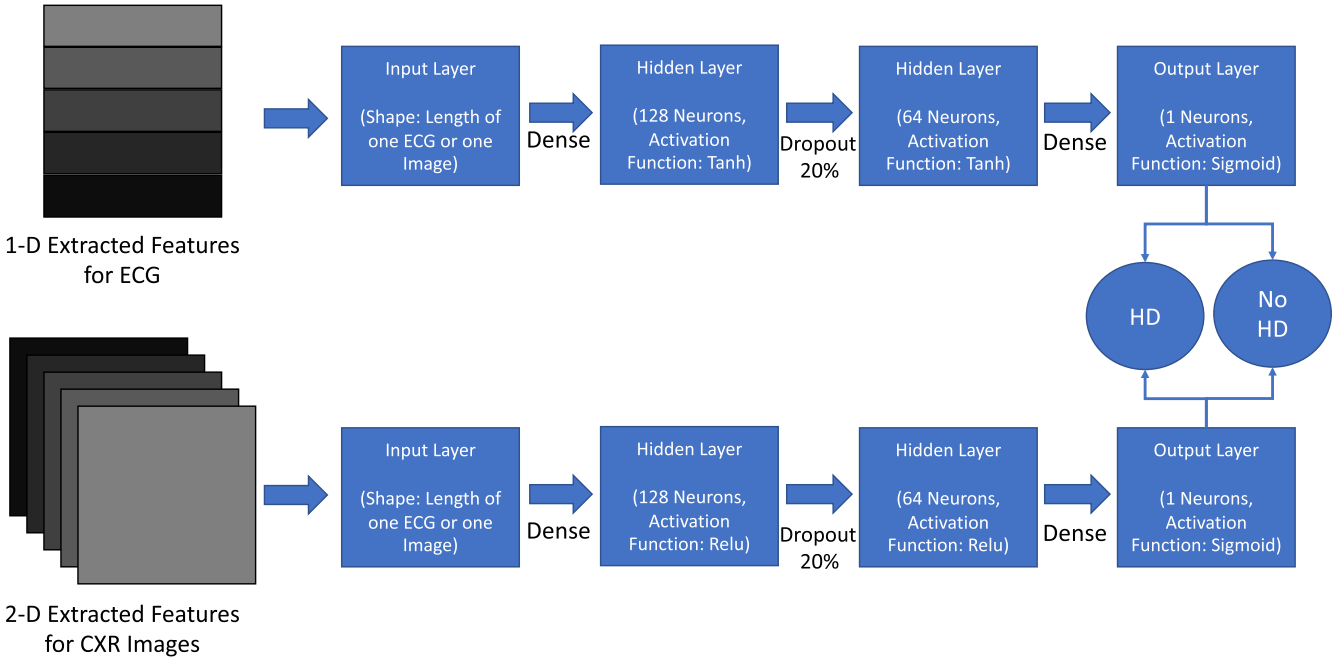

FIGURE 4. 1-D and 2-D model architecture.

A. TOPSIS ALGORITHM

TOPSIS ranks models by calculating each model's proximity to an "ideal" solution (highest possible values for each metric) and distance from an "anti-ideal" solution (lowest values). After normalizing and weighting the metrics, TOPSIS calculates the Euclidean distance from both ideal and anti-ideal points, ranking models based on their relative closeness to the ideal solution.

B. MULTIPLE REGRESSION ANALYSIS (MRA)

MRA assigns weights to each metric (accuracy, F1 score, and AUC) based on their contribution to the model's overall ranking score. This aggregated score for each model is calculated by multiplying each metric by its weight, providing a ranked list where higher scores indicate better performance [44].

C. RANKING RESULTS

Both TOPSIS and MRA yielded similar top-ranking models, depicted in tables 6, 7 for ECG and table 8 for CXR Images, ensuring consistency in selecting the best-performing model for accurate, efficient HD classification.

D. ECG RESULTS

The results for the classification of ECG Signals using various different ML and DL models are demonstrated in Table 6 and Table 7 and the learning curves are illustrated in Figures 7b - 7e. Both ML and DL models employing the circular convolution method for feature extraction achieved high performance, with CNN reaching an accuracy of approximately 94%, an F1 score of 0.94, and an AUC value of 0.98. These results highlight that the proposed feature extraction method not only enhances processing speed but also delivers excellent accuracy in classification.

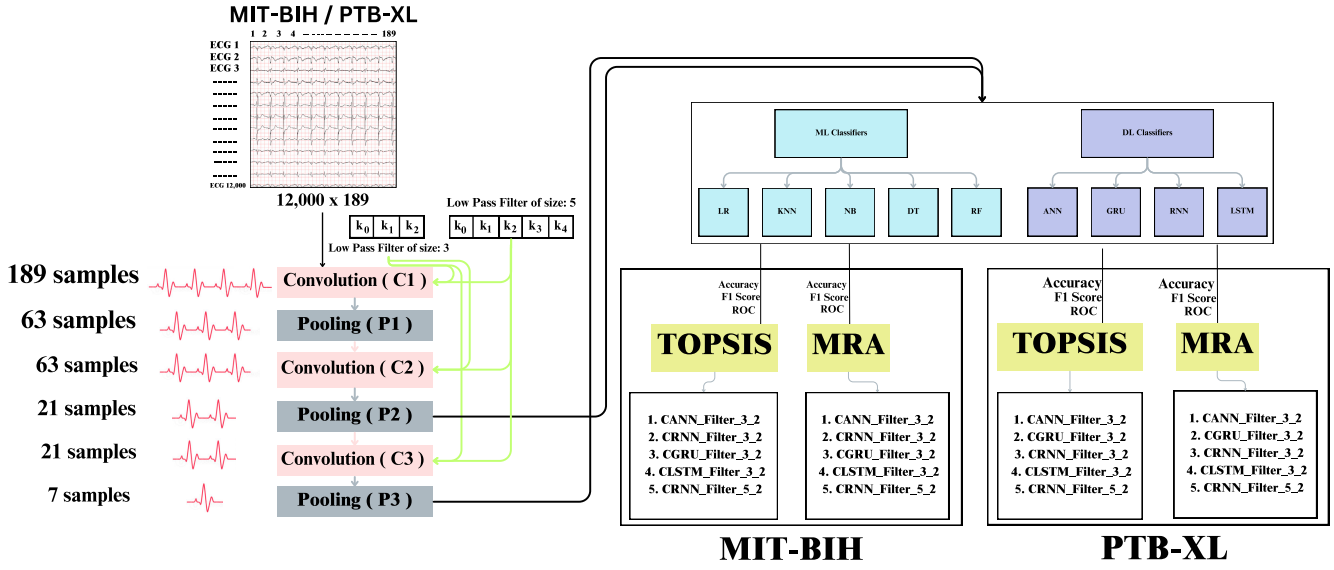

FIGURE 5. 1-D model development with features extraction and model ranking.

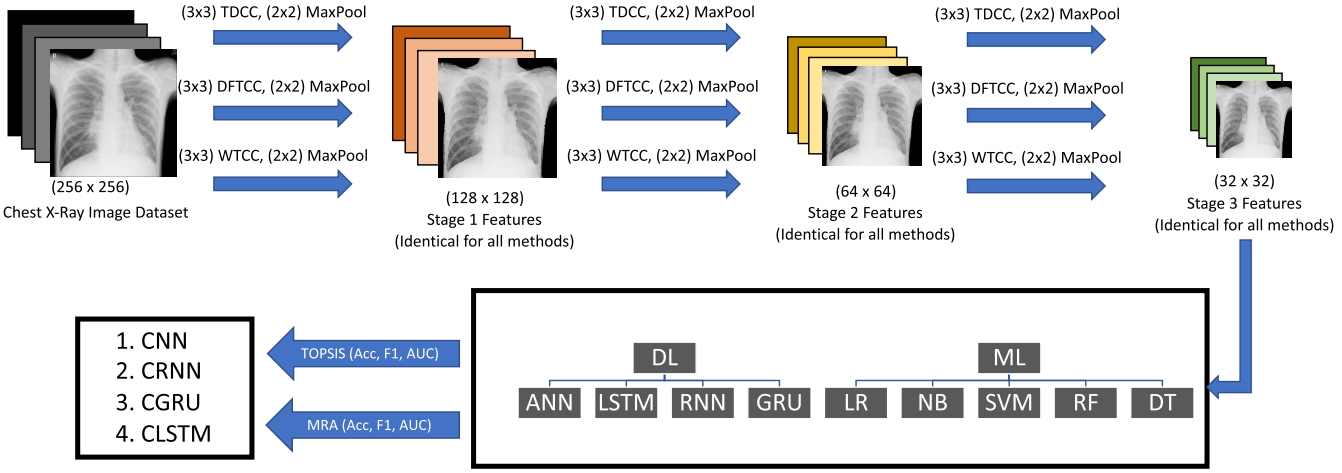

FIGURE 6. 2-D model development with features extraction and model ranking.

E. CXR IMAGE

The results for the classification of CXR Images using various different ML and DL models are demonstrated in Table 8 and the learning curves are illustrated in Figures 8b - 8e. Both ML and DL models that utilized the circular convolution method for feature extraction demonstrated high performance. Specifically, the CNN model achieved an accuracy of approximately 94%, precision of 0.95, recall of 0.92, F1 score of 0.94, and an AUC value of 0.98. These findings underscore the proposed feature extraction method's ability to significantly enhance processing speed—up to 4.5 times faster than the traditional TD method—while maintaining high classification accuracy. This efficiency offers considerable time savings without compromising on accuracy, making it highly effective for 2-D image-based HD classification.

F. ANALYSIS OF RESULTS AND FINDINGS FROM THE INVESTIGATION

1) 1-D ECG

Following the extraction of features, the obtained features after Stage 2 and Stage 3 Convolution and Polling were classified using various ML and DL models and each model's accuracy, f1 score, AUC values were observed and depicted in Tables 6 and 7. Though all the DL models performed relatively quite, underscoring the quality of extracted features, the proposed CNN model achieved the highest overall performance.

To evaluate the proposed model's performance under different data distributions, such as low class imbalance, high class imbalance, small data size, etc., were also employed. The model's accuracy dipped for these different distributions. This is a major issue in DL models because if the dataset

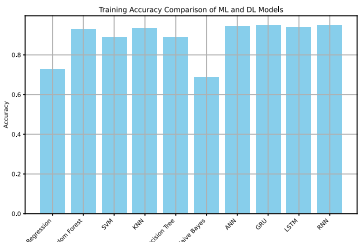

(a) Training Accuracy Comparison of ML and DL

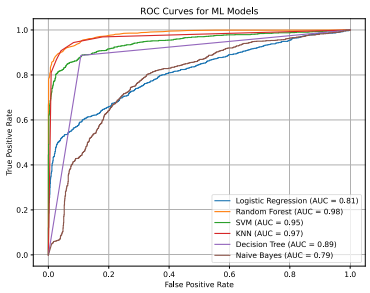

(b) ROC Curves for ML Models

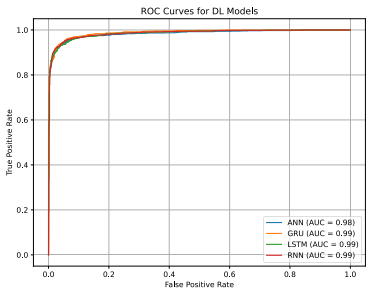

(c) ROC Curves for DL Models

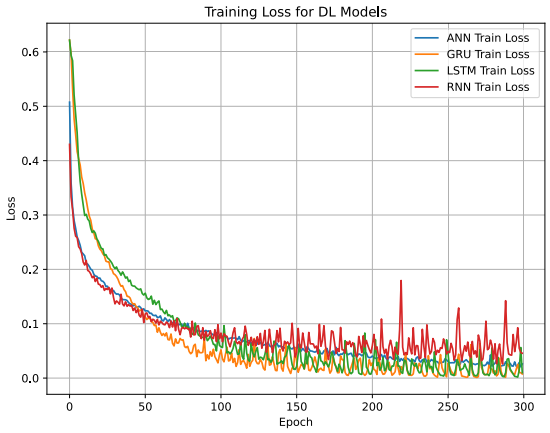

(d) Training Loss for DL Models

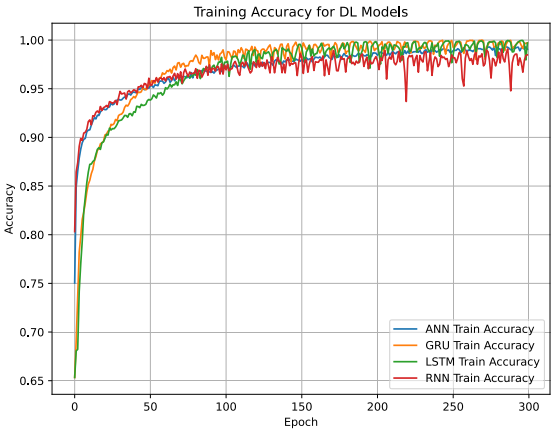

(e) Training Accuracy for DL Models

FIGURE 7. **Comparative analysis of ml and dl models for MIT-BIH dataset classification.**

TABLE 5. **Performance metrics for different distributions of MIT-BIH dataset with class imbalance.**

Dataset	Acc	Precision	Recall	F1	AUC
Dataset_8000_6400	82.5%	0.52	0.42	0.46	0.70
Dataset_8000_1150	87.0%	0.74	0.58	0.65	0.75
Dataset_5000_4500	90.2%	0.38	0.28	0.32	0.65
Dataset_1000_750	78.0%	0.57	0.50	0.53	0.72

is highly imbalanced, the model learns to favor the majority class. Or the model has fewer examples to learn meaningful patterns from the minority class. Standard loss functions like cross-entropy, which is used in the proposed method assume balanced classes. If the dataset is imbalanced, the model may minimize loss by always predicting the majority class. It can be observed from Table 5 and Figure 9 where Dataset followed by the total number of samples and number of samples for Non-HD class is listed shows the performance of the proposed model for class imbalance with the presence of noise and smaller data size. The proposed model performs reasonably well for imbalanced classes. However, it is evident that datasets with extreme imbalance (Dataset-5000-4500) result in higher accuracy but suffer from lower recall for the minority class, whereas datasets with a more balanced distribution (Dataset-1000-750) achieve better overall F1 scores. This highlights the trade-off between class representation and model performance. Additionally, the AUC values indicate that the model maintains decent discriminatory power across datasets, though performance varies based on sample size and noise levels. Future works can lead to a model that handles the class imbalance more robustly by implementing Balanced Loss Functions or Focal Loss to give more importance to the minority class or by using Ensemble Methods such as Balanced Random Forest, XGBoost with class weights. Data Augmentation, which was used by [14] is also an effective approach to handling class imbalance in ECG-based HD Detection.

2) 2-D CXR IMAGES

Just as for 1-D ECG, the extracted features from convolution and pooling was used for extensive development of ML and DL models for classification of HD from CXR images. Every model's accuracy, f1 score and AUC was observed and ranked and the results are shown in Table 8. The proposed CNN model using WT-based circular convolution had the highest overall accuracy, precision, recall, f1 score and AUC values.

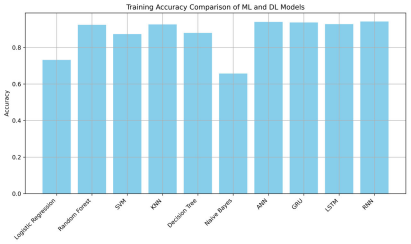

(a) Training Accuracy Comparison of ML and DL Models for CXR Images

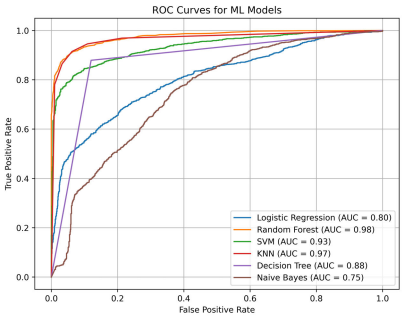

(b) ROC Curves for ML Models for CXR Images

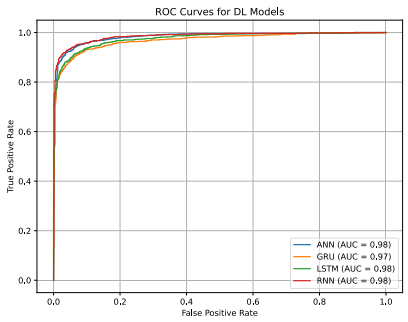

(c) ROC Curves for DL Models for CXR Images

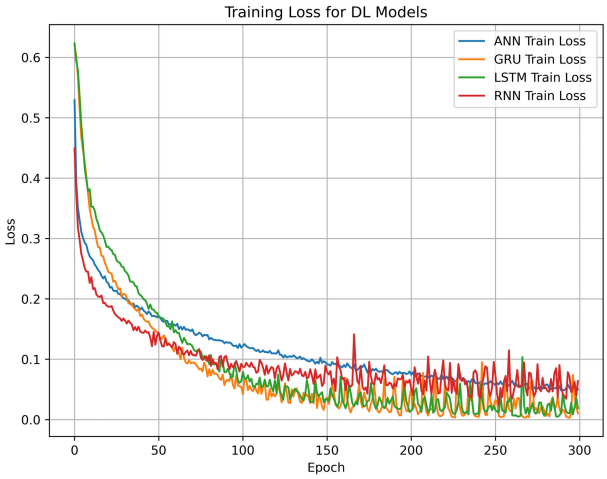

(d) Training Loss for DL Models for CXR Images

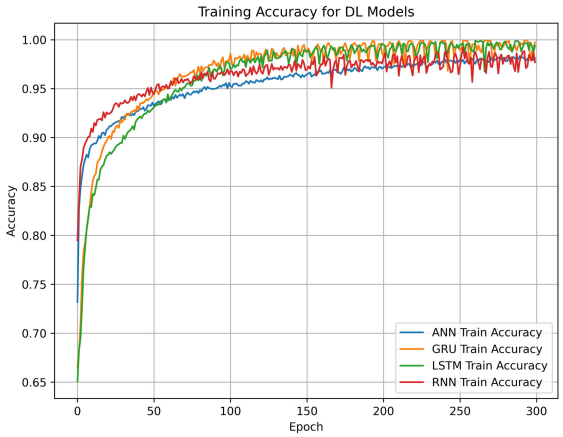

(e) Training Accuracy for DL Models for CXR Images

FIGURE 8. Performance evaluation of ML and DL models for CXR image dataset classification.

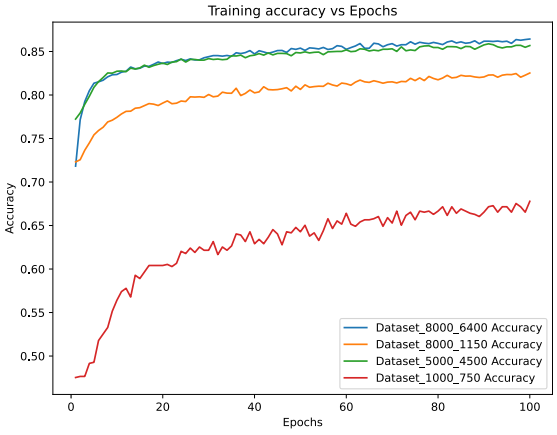

FIGURE 9. Model performance for distributions of data.

TABLE 6. Combined ML and DL model rankings for stage 2 and stage 3 based on accuracy, F1 Score, and ROC AUC for MIT-BIH dataset.

Model	Stage 2			Stage 3		
	Acc	F1	AUC	Acc	F1	AUC
CNN	0.95	0.95	0.99	0.88	0.88	0.94
CRNN	0.95	0.95	0.99	0.88	0.88	0.94
CGRU	0.95	0.95	0.98	0.88	0.88	0.94
CLSTM	0.94	0.94	0.99	0.87	0.87	0.94
CRF	0.93	0.93	0.98	0.88	0.88	0.95
CKNN	0.93	0.93	0.97	0.88	0.88	0.94
CSVM	0.89	0.88	0.95	0.80	0.79	0.87
CDT	0.89	0.89	0.89	0.83	0.83	0.83
CLR	0.73	0.71	0.81	0.69	0.67	0.72
CNB	0.69	0.62	0.79	0.66	0.58	0.73

X. RESEARCH CONTRIBUTION

In case of ECG-based detection of HD standard MIT-BIH and PTB data has been used in the simulation study. The detection technique employed in this case is CNN. The total time of detection is very important as it guides whether the proposed method can be employed for online detection of HD. The time taken for the development of the detection model comprises of sum of Feature Extraction time and training time. In the present case, the features from the full raw dataset have been extracted by three direct convolution methods, Time Domain, DFT and proposed Winograd method. Observation

TABLE 7. Combined ML and DL model rankings for stage 2 and stage 3 based on accuracy, F1 score, and ROC AUC for PTB-XL dataset.

Model	Stage 2			Stage 3		
	Acc	F1	AUC	Acc	F1	AUC
CNN	0.94	0.94	0.98	0.87	0.90	0.92
CGRU	0.93	0.94	0.97	0.88	0.88	0.93
CLSTM	0.93	0.92	0.96	0.88	0.87	0.94
CRF	0.92	0.92	0.95	0.89	0.89	0.94
CRNN	0.91	0.90	0.93	0.86	0.86	0.92
CKNN	0.89	0.89	0.92	0.85	0.84	0.91
CSVM	0.87	0.87	0.90	0.81	0.80	0.88
CDT	0.86	0.85	0.88	0.82	0.82	0.85
CNB	0.73	0.71	0.80	0.70	0.68	0.75
CLR	0.72	0.70	0.82	0.66	0.65	0.72

TABLE 8. Model rankings based on accuracy, precision, recall, F1 Score, and ROC AUC for CXR images features extracted by 3-stage C+P.

Model	Acc	Precision	Recall	F1	AUC
CNN	0.98	0.95	0.93	0.95	0.98
CRNN	0.97	0.93	0.91	0.92	0.98
CGRU	0.99	0.91	0.89	0.92	0.97
CLSTM	0.99	0.90	0.91	0.92	0.98
CRF	0.92	0.89	0.88	0.90	0.93
CKNN	0.92	0.90	0.88	0.91	0.92
CSVM	0.87	0.85	0.82	0.87	0.90
CDT	0.87	0.84	0.83	0.85	0.88
CLR	0.73	0.71	0.69	0.71	0.80
CNB	0.65	0.66	0.64	0.70	0.82

of the results presented in Table 2 reveals that further full MIT-BIH Dataset, the time taken for features extraction using 3-point convolution are 5.35 seconds, 8.84 seconds and 1.87 seconds using Conventional Time Domain, DFT-based approach and WT-based approach respectively. Hence, the total times taken for features extraction by WT method is 2.86 and 4.73 times faster than conventional convolution and DFT based approach respectively. Thus the novelty and the strength of the proposed method on this proposed paper is: substantial saving in both feature extraction time and total time of development of the model. It is a substantial saving in time which accelerates the development of DL models for disease detection. This saving in time can be immensely beneficiary in real-time applications.

XI. SUMMARY AND CONCLUSION

This research underscores the potential of WT-based circular convolution for accelerating HD detection in ECG and CXR datasets. By addressing the computational constraints inherent in traditional convolution methods, our proposed WT-based approach delivers substantial improvements in processing time, making it highly applicable to time-sensitive medical diagnostics. The WT method achieved notable efficiency gains—approximately 2.86x and 4.73x over time-domain and DFT methods, respectively, in ECG signal processing, and similar gains, upto 4.5x faster model development in CXR image classification. These advancements enable DL models to retain high accuracy while reducing training and inference times, a critical requirement for real-time clinical decision-making. Since, the proposed method offers substantial savings in model development time. The challenges in model development have been overcome in the proposed approach and thus, future work could extend the WT methodology to other medical imaging modalities and further explore its integration with IoT-based commercial devices, portable HD Detection models as well as model deployment in cloud-based applications.

APPENDIX A
MATHEMATICAL ILLUSTRATION OF 1-D CONVOLUTION METHODOLOGIES USED IN THE STUDY

A. TIME DOMAIN CIRCULAR CONVOLUTION EXAMPLE ILLUSTRATION

In this appendix, we present the step-by-step calculation for time-domain circular convolution using the sequences $s[n] = [3, 2, 5]$ and $k[n] = [-1, 1, 2]$. Circular convolution treats sequences as periodic and computes the result by constructing a circular matrix from the input sequence, followed by element-wise multiplication with the kernel sequence.

1) CIRCULAR MATRIX CONSTRUCTION

The first step is to construct the circular matrix for $s[n] = [3, 2, 5]$, where each row is a circularly shifted version of the sequence. The resulting circular matrix C is:

$$C = \begin{bmatrix} 3 & 5 & 2 \\ 2 & 3 & 5 \\ 5 & 2 & 3 \end{bmatrix}$$

2) MATRIX MULTIPLICATION WITH KERNEL SEQUENCE

Next, we perform element-wise multiplication between each row of the circular matrix C and the kernel sequence $k[n] = [-1, 1, 2]$. The output sequence $t[n]$ is obtained by summing the products for each row.

a: STEP 1: FIRST ROW OF C

For the first row of C:

$$\begin{aligned}[3, 5, 2] \cdot [-1, 1, 2] &= (3 \times -1) + (5 \times 1) + (2 \times 2) \\ &= -3 + 5 + 4 = 6\end{aligned}$$

b: STEP 2: SECOND ROW OF C

For the second row of C:

$$\begin{aligned}[2, 3, 5] \cdot [-1, 1, 2] &= (2 \times -1) + (3 \times 1) + (5 \times 2) \\ &= -2 + 3 + 10 = 11\end{aligned}$$

c: STEP 3: THIRD ROW OF C

For the third row of C:

$$\begin{aligned}[5, 2, 3] \cdot [-1, 1, 2] &= (5 \times -1) + (2 \times 1) + (3 \times 2) \\ &= -5 + 2 + 6 = 3\end{aligned}$$

3) FINAL CIRCULAR CONVOLUTION OUTPUT

The result of the circular convolution is the sequence $z[n] = [6, 11, 3]$. This output is derived by summing the element-wise products of each row of the circular matrix with the kernel sequence. Therefore, the output sequence $z[n]$ is:

$$z[n] = [6, 11, 3]$$

B. DFT-BASED CIRCULAR CONVOLUTION EXAMPLE ILLUSTRATION

In this appendix, we detail the calculation of circular convolution using the DFT and its inverse. The sequences used in this example are $s[n] = [3, 2, 5]$ and $h[n] = [-1, 1, 2]$.

1) DFT CALCULATION

We begin by calculating the DFT of the input sequence $s[n]$ and the filter sequence $h[n]$. The DFT converts the time-domain sequences into the frequency domain. For a sequence $x[n]$ of length N, the DFT is defined as:

$$X[k] = \sum_{n=0}^{N-1} x[n] \cdot e^{-j\frac{2\pi kn}{N}}$$

DFT of the Input Sequence $s[n]$

For the input sequence $s[n] = [3, 2, 5]$, the DFT is computed as follows:

$$S[k] = \left[S[0], S[1], S[2]\right]$$

Calculating each component:

$$\begin{aligned}
S[0] &= 3 \cdot e^{-j0} + 2 \cdot e^{-j0} + 5 \cdot e^{-j0} = 3 + 2 + 5 = 10, \\
S[1] &= 3 \cdot e^{-j0} + 2 \cdot e^{-j\frac{2\pi}{3}} + 5 \cdot e^{-j\frac{4\pi}{3}} \\
&= 0.5 - j \cdot 2.598, \\
S[2] &= 3 \cdot e^{-j0} + 2 \cdot e^{-j\frac{4\pi}{3}} + 5 \cdot e^{-j\frac{8\pi}{3}} \\
&= 0.5 + j \cdot 2.598.
\end{aligned}$$

Thus, the DFT of $s[n]$ is:

$$S[k] = \left[10,\ 0.5 - j \cdot 2.598,\ 0.5 + j \cdot 2.598\right]$$

a: DFT OF THE FILTER SEQUENCE H[N]

Next, we compute the DFT of the filter sequence $h[n] = [-1, 1, 2]$:

$$H[k] = \left[H[0], H[1], H[2]\right]$$

Calculating each component:

$$\begin{aligned}
H[0] &= -1 + 1 + 2 = 2, \\
H[1] &= -1 \cdot e^{-j0} + 1 \cdot e^{-j\frac{2\pi}{3}} + 2 \cdot e^{-j\frac{4\pi}{3}} \\
&= 2.5 + j \cdot 0.866, \\
H[2] &= -1 + 1 \cdot e^{-j\frac{4\pi}{3}} + 2 \cdot e^{-j\frac{8\pi}{3}} \\
&= 2.5 - j \cdot 0.866.
\end{aligned}$$

Thus, the DFT of $k[n]$ is:

$$H[k] = \left[2,\ 2.5 + j \cdot 0.866,\ 2.5 - j \cdot 0.866\right]$$

2) POINTWISE MULTIPLICATION IN THE DFT DOMAIN

After obtaining the DFTs $S[k]$ and $H[k]$, we perform pointwise multiplication:

$$t[k] = S[k] \cdot H[k]$$

Calculating each component:

$$\begin{aligned}
Y[0] &= S[0] \cdot K[0] = 10 \cdot 2 = 20, \\
Y[1] &= (0.5 + j\frac{\sqrt{3}}{2}) \cdot (2.5 + j \cdot 0.866) \\
&= -1 - j \cdot 6.928, \\
Y[2] &= (0.5 - j\frac{\sqrt{3}}{2}) \cdot (2.5 - j \cdot 0.866) \\
&= -1 + j \cdot 6.928.
\end{aligned}$$

Thus, the DFT of the output sequence is:

$$T[k] = \left[20, -1 - j \cdot 6.928, -1 + j \cdot 6.928\right]$$

3) INVERSE DFT (IDFT)

To transform the result back to the time domain, we compute the Inverse DFT (IDFT), defined as:

$$t[n] = \frac{1}{N} \sum_{k=0}^{N-1} Y[k] \cdot e^{j\frac{2\pi kn}{N}}$$

For $N = 3$, the result is calculated as follows:

$$\begin{aligned}
t[0] &= \frac{1}{3}\left(20 + (-1 - j \cdot 6.928) + (-1 + j \cdot 6.928)\right) = 6 \\
t[1] &= \frac{1}{3}\left(20 + (-1 - j \cdot 6.928)e^{j\frac{2\pi}{3}}\right. \\
&\qquad \left. + (-1 + j \cdot 6.928)e^{j\frac{4\pi}{3}}\right) = 11 \\
t[2] &= \frac{1}{3}\left(20 + (-1 - j \cdot 6.928)e^{j\frac{4\pi}{3}}\right. \\
&\qquad \left. + (-1 + j \cdot 6.928)e^{j\frac{8\pi}{3}}\right) = 3
\end{aligned}$$

Thus, the final result of the circular convolution in the time domain is:

$$t[n] = [6, 11, 3]$$

This matches the result obtained from the time-domain circular convolution method, verifying the correctness of the DFT-based approach.

4) EFFICIENCY OF DFT-BASED CIRCULAR CONVOLUTION

The DFT-based approach to circular convolution, while requiring additional transformations (i.e., the DFT and the IDFT), brings substantial computational benefits, particularly when dealing with long input signals.

The time-domain circular convolution method typically has a computational complexity of $O(N^2)$, where N is the

length of the input sequence. This quadratic complexity arises because each element of the output sequence requires a full summation over all elements of the input sequences.

In contrast, the DFT-based circular convolution significantly reduces this complexity by transforming the convolution operation into the frequency domain. Using the DFT, the convolution is converted into a pointwise multiplication, which simplifies the operation considerably. By utilizing the Fast Fourier Transform (FFT) algorithm, the computational complexity of the DFT can be reduced from $O(N^2)$ to $O(N \log N)$, providing a substantial improvement in efficiency.

After performing the pointwise multiplication in the frequency domain, the result is transformed back into the time domain using the IDFT. Although these additional transformations (DFT and IDFT) introduce some overhead, the overall reduction in complexity more than compensates for this, particularly for longer sequences.

For applications involving long signals, such as ECG recordings, which can consist of thousands of data points, the DFT-based approach is highly advantageous. The improved efficiency ensures faster processing and enables the application of more complex models to real-time or near real-time signal analysis tasks.

C. WINOGRAD BASED CIRCULAR CONVOLUTION EXAMPLE ILLUSTRATION

The Winograd algorithm efficiently computes small-point DFT and its inverse. In this example, we use Winograd's algorithm for 3-point circular convolution, with $\mathbf{s} = [3, 2, 5]$ and $\mathbf{h} = [-1, 1, 2]$. We calculate the DFT for each sequence, multiply the results pointwise, and then apply the Inverse DFT to obtain the convolution. The result will match the time-domain and standard DFT-based convolutions.

a: STEP 1: COMPUTE DFT USING WINOGRAD'S ALGORITHM

Using the precomputed constants $\cos\left(\frac{2\pi}{3}\right) = -0.5$ and $\sin\left(\frac{2\pi}{3}\right) = 0.866$, we compute the DFT for each sequence:

b: INPUT SEQUENCE DFT

For $\mathbf{s} = [3, 2, 5]$:

$$\begin{aligned} t_1 &= s[1] + s[2] = 2 + 5 = 7 \\ m_0 &= s[0] + t_1 = 3 + 7 = 10 \\ m_1 &= (-0.5 - 1) \cdot t_1 = (-1.5) \cdot 7 = -10.5 \\ m_2 &= j \cdot 0.866 \cdot (s[1] - s[2]) = j \cdot 0.866 \cdot (2 - 5) = -j \cdot 2.598 \end{aligned}$$

Thus, the DFT of $\mathbf{s}$ is:

$$\begin{aligned} S[0] &= m_0 = 10 \\ S[1] &= m_0 + m_1 + m_2 = 10 + (-10.5) \\ &\quad -j \cdot 2.598 = 0.5 - j \cdot 2.598 \\ S[2] &= m_0 + m_1 - m_2 = 10 + (-10.5) \\ &\quad +j \cdot 2.598 = 0.5 + j \cdot 2.598 \end{aligned}$$

c: FILTER SEQUENCE DFT

For $\mathbf{h} = [-1, 1, 2]$:

$$\begin{aligned} t_1 &= h[1] + h[2] = 1 + 2 = 3 \\ m_0 &= h[0] + t_1 = -1 + 3 = 2 \\ m_1 &= (-0.5 - 1) \cdot t_1 = (-0.5) \cdot 3 = -4.5 \\ m_2 &= j \cdot 0.866 \cdot (h[1] - h[2]) \\ &= j \cdot 0.866 \cdot (1 - 2) = -j \cdot 0.866 \end{aligned}$$

Thus, the DFT of $\mathbf{h}$ is:

$$\begin{aligned} H[0] &= m_0 = 2 \\ H[1] &= m_0 + m_1 + m_2 = 2 + (-4.5) \\ &\quad -j \cdot 0.866 = 2.5 - j \cdot 0.866 \\ H[2] &= m_0 + m_1 - m_2 = 2 + (-4.5) \\ &\quad +j \cdot 0.866 = 2.5 + j \cdot 0.866 \end{aligned}$$

d: STEP 2: POINTWISE MULTIPLICATION

We now perform pointwise multiplication of the DFTs $S[k]$ and $H[k]$.

$$\begin{aligned} Y[0] &= S[0] \cdot H[0] = 10 \cdot 2 = 20 \\ Y[1] &= S[1] \cdot H[1](0.5 - j \cdot 2.598) \cdot (2.5 - j \cdot 0.866) \\ Y[1] &= -1 - j \cdot 6.928 \\ Y[2] &= (0.5 + j \cdot 2.598) \cdot (2.5 + j \cdot 0.866) \\ Y[2] &= -1 + j \cdot 6.928 \end{aligned}$$

Thus, the pointwise multiplication result is:

$$Y[k] = [20, -1 - j \cdot 6.928, -1 + j \cdot 6.928]$$

e: STEP 3: COMPUTE INVERSE DFT USING WINOGRAD'S ALGORITHM

For the sequence $Y[k] = [20, -1 - j \cdot 6.928, -1 + j \cdot 6.928]$, use the same precomputed constants:

$$\begin{aligned} t_1 &= Y[1] + Y[2] = (-1 - j \cdot 6.928) + (-1 + j \cdot 6.928) = -2 \\ m_0 &= Y[0] + t_1 = 20 + (-2) = 18 \\ m_1 &= (-0.5 - 1) \cdot (-2) = 3 \\ m_2 &= j \cdot 0.866 \cdot [(-1 - j \cdot 6.928) - (-1 + j \cdot 6.928)] \\ &= j \cdot 0.866 \cdot (-j \cdot 13.856) = 12 \end{aligned}$$

Now compute the IDFT results as:

$$\begin{aligned} y[0] &= m_0 = 18 \\ y[1] &= m_0 + m_1 - m_2 = 18 + 3 - 12 = 9 \\ y[2] &= m_0 + m_1 + m_2 = 18 + 3 + 12 = 33 \end{aligned}$$

f: STEP 4: NORMALIZE THE SEQUENCE

Now normalize each element by dividing by $N = 3$:

$$\begin{aligned} y_{\text{normalized}}[0] &= \frac{18}{3} = 6 \\ y_{\text{normalized}}[1] &= \frac{9}{3} = 3 \\ y_{\text{normalized}}[2] &= \frac{33}{3} = 11 \end{aligned}$$

APPENDIX B
ILLUSTRATION OF 2-D CIRCULAR CONVOLUTION METHODOLOGY USED IN THE STUDY

A. 2-D TD CIRCULAR CONVOLUTION

In this example, we performed 2D time-domain circular convolution on a 3×3 image matrix A and a 3×3 filter matrix B exactly how it is used in this study.

The input image A is:

$$A = \begin{bmatrix} 1 & 2 & 3 \\ 4 & 5 & 6 \\ 7 & 8 & 9 \end{bmatrix}$$

The filter B is:

$$B = \begin{bmatrix} 5 & 6 & 7 \\ 8 & 9 & 10 \\ 11 & 12 & 13 \end{bmatrix}$$

a: CIRCULAR MATRIX CONSTRUCTION

To perform circular convolution, the image A is first transformed into a circulant matrix C_A as follows:

$$C_A = \begin{bmatrix} 1 & 2 & 3 & 4 & 5 & 6 & 7 & 8 & 9 \\ 4 & 5 & 6 & 7 & 8 & 9 & 1 & 2 & 3 \\ 7 & 8 & 9 & 1 & 2 & 3 & 4 & 5 & 6 \\ 2 & 3 & 1 & 5 & 6 & 4 & 8 & 9 & 7 \\ 5 & 6 & 4 & 8 & 9 & 7 & 2 & 3 & 1 \\ 8 & 9 & 7 & 2 & 3 & 1 & 5 & 6 & 4 \\ 3 & 1 & 2 & 6 & 4 & 5 & 9 & 7 & 8 \\ 6 & 4 & 5 & 9 & 7 & 8 & 3 & 1 & 2 \\ 9 & 7 & 8 & 3 & 1 & 2 & 6 & 4 & 5 \end{bmatrix}$$

The filter B is flattened into a vector:

$$B_{\text{flat}} = [5, 6, 7, 8, 9, 10, 11, 12, 13]$$

b: CIRCULAR CONVOLUTION CALCULATION

The convolution is performed by multiplying each row of C_A with the flattened filter B_{flat}. The result for each row is computed as follows:

$$\begin{aligned}
&\text{Row 1: } (1 \times 5) + (2 \times 6) + (3 \times 7) + \cdots + (9 \times 13) = 435 \\
&\text{Row 2: } (4 \times 5) + (5 \times 6) + (6 \times 7) + \cdots + (3 \times 13) = 435 \\
&\text{Row 3: } (7 \times 5) + (8 \times 6) + (9 \times 7) + \cdots + (6 \times 13) = 426 \\
&\text{Row 4: } (2 \times 5) + (3 \times 6) + (1 \times 7) + \cdots + (7 \times 13) = 435 \\
&\text{Row 5: } (5 \times 5) + (6 \times 6) + (4 \times 7) + \cdots + (1 \times 13) = 435 \\
&\text{Row 6: } (8 \times 5) + (9 \times 6) + (7 \times 7) + \cdots + (4 \times 13) = 426 \\
&\text{Row 7: } (3 \times 5) + (1 \times 6) + (2 \times 7) + \cdots + (8 \times 13) = 354 \\
&\text{Row 8: } (6 \times 5) + (4 \times 6) + (5 \times 7) + \cdots + (2 \times 13) = 354 \\
&\text{Row 9: } (9 \times 5) + (7 \times 6) + (8 \times 7) + \cdots + (5 \times 13) = 345
\end{aligned}$$

c: FINAL CONVOLUTION RESULT

The final result of the 2D circular convolution is:

$$C_{\text{result}} = \begin{bmatrix} 435 & 435 & 426 \\ 435 & 435 & 426 \\ 354 & 354 & 345 \end{bmatrix}$$

B. 2-D DFT CIRCULAR CONVOLUTION EXAMPLE ILLUSTRACTION

Let matrix A and filter B be:

$$A = \begin{bmatrix} 1 & 2 & 3 \\ 4 & 5 & 6 \\ 7 & 8 & 9 \end{bmatrix}, \quad B = \begin{bmatrix} 5 & 6 & 7 \\ 8 & 9 & 10 \\ 11 & 12 & 13 \end{bmatrix}$$

1) STEP 1: COMPUTE THE 2D DFT OF BOTH MATRICES

We first calculate the 2D DFT of matrix A by performing the row-wise and column-wise 1D DFTs.

a: ROW-WISE DFT FOR A

DFT of rows:

$$\begin{aligned}
A_{\text{row1}} &= [6, -1.5 + 0.866j, -1.5 - 0.866j] \\
A_{\text{row2}} &= [15, -1.5 + 0.866j, -1.5 - 0.866j] \\
A_{\text{row3}} &= [24, -1.5 + 0.866j, -1.5 - 0.866j]
\end{aligned}$$

b: COLUMN-WISE DFT FOR A

DFT of columns:

$$\begin{aligned}
A_{\text{col1}} &= [45, -13.5 + 7.794j, -13.5 - 7.794j] \\
A_{\text{col2}} &= [-4.5 + 2.598j, 0, 0] \\
A_{\text{col3}} &= [-4.5 - 2.598j, 0, 0]
\end{aligned}$$

Thus, the 2D DFT of matrix A is:

$$A_{\text{DFT}} = \begin{bmatrix} 45 & -4.5 + 2.598j & -4.5 - 2.598j \\ -13.5 + 7.794j & 0 & 0 \\ -13.5 - 7.794j & 0 & 0 \end{bmatrix}$$

c: ROW-WISE AND COLUMN-WISE DFT FOR B

Similarly, the 2D DFT for matrix B is calculated as:

$$B_{\text{DFT}} = \begin{bmatrix} 81 & -4.5 + 2.598j & -4.5 - 2.598j \\ -13.5 + 7.794j & 0 & 0 \\ -13.5 - 7.794j & 0 & 0 \end{bmatrix}$$

2) STEP 2: ELEMENT-WISE MULTIPLICATION IN FREQUENCY DOMAIN

We now perform element-wise multiplication of the corresponding elements of A_{DFT} and B_{DFT}:

$$\text{Result}_{\text{DFT}} = \begin{bmatrix} A_{11}B_{11} & A_{12}B_{12} & A_{13}B_{13} \\ A_{21}B_{21} & A_{22}B_{22} & A_{23}B_{23} \\ A_{31}B_{31} & A_{32}B_{32} & A_{33}B_{33} \end{bmatrix}$$

This gives us:

$$\text{Result}_{\text{DFT}} = \begin{bmatrix} 3645 & 18 + 23.382j & 18 - 23.382j \\ 162 + 210.438j & 0 & 0 \\ 162 - 210.438j & 0 & 0 \end{bmatrix}$$

3) STEP 3: APPLY THE INVERSE DFT

Now we apply the inverse DFT to the resulting matrix, firstly row-wise, then column wise, as done previously to get the final result in the spatial domain:

$$\text{Final result} = \begin{bmatrix} 435 & 435 & 426 \\ 435 & 435 & 426 \\ 354 & 354 & 345 \end{bmatrix}$$

Thus, the final result of circular convolution using the DFT method matches the time-domain method.

C. 2-D WINOGRAD DFT CIRCULAR CONVOLUTION EXAMPLE ILLUSTRATION

Let matrix A and filter B be:

$$A = \begin{bmatrix} 1 & 2 & 3 \\ 4 & 5 & 6 \\ 7 & 8 & 9 \end{bmatrix}, \quad B = \begin{bmatrix} 5 & 6 & 7 \\ 8 & 9 & 10 \\ 11 & 12 & 13 \end{bmatrix}$$

1) STEP 1: COMPUTE THE 2D DFT OF BOTH MATRICES USING WINOGRAD'S METHOD

We calculate the 2D Winograd DFT for A by performing row-wise and column-wise 1D Winograd DFTs.

a: ROW-WISE WINOGRAD DFT FOR A

Using Winograd's method for 1D DFT on row $A_{\text{row1}} = [1, 2, 3]$:

1. Compute intermediate terms:

$$t_1 = A[1] + A[2] = 5$$

2. Compute DC component:

$$W_0 = A[0] + t_1 = 6$$

3. Cosine and sine terms:

$$W_1 = W_0 + (-1.5) + (-0.866j) = -1.5 - 0.866j$$
$$W_2 = W_0 + (-1.5) + (0.866j) = -1.5 + 0.866j$$

This results in:

$$A_{\text{row1}} = [6, -1.5 - 0.866j, -1.5 + 0.866j]$$

Similarly, we calculate for the remaining rows:

$$A_{\text{row2}} = [15, -1.5 - 0.866j, -1.5 + 0.866j]$$
$$A_{\text{row3}} = [24, -1.5 - 0.866j, -1.5 + 0.866j]$$

b: COLUMN-WISE WINOGRAD DFT FOR A

Following the same method, we compute column-wise DFTs, giving:

$$A_{\text{DFT}} = \begin{bmatrix} 45 & -4.5 + 2.598j & -4.5 - 2.598j \\ -13.5 + 7.794j & 0 & 0 \\ -13.5 - 7.794j & 0 & 0 \end{bmatrix}$$

Similarly, the 2D DFT for B using Winograd's method is:

$$B_{\text{DFT}} = \begin{bmatrix} 81 & -4.5 + 2.598j & -4.5 - 2.598j \\ -13.5 + 7.794j & 0 & 0 \\ -13.5 - 7.794j & 0 & 0 \end{bmatrix}$$

2) STEP 2: ELEMENT-WISE MULTIPLICATION IN FREQUENCY DOMAIN

We multiply corresponding elements of A_{DFT} and B_{DFT}:

$$\text{Result}_{\text{DFT}} = \begin{bmatrix} 3645 & 18 + 23.382j & 18 - 23.382j \\ 162 + 210.438j & 0 & 0 \\ 162 - 210.438j & 0 & 0 \end{bmatrix}$$

3) STEP 3: APPLY THE INVERSE WINOGRAD DFT

Applying the inverse Winograd DFT yields the spatial domain result:

To compute the inverse DFT, apply the WT with respect to the row, then with respect to the column using WT formula. After normalizing the obtained values (dividing it by 9, in this case), the final result is obtained.

$$\text{Final result} = \begin{bmatrix} 435 & 435 & 426 \\ 435 & 435 & 426 \\ 354 & 354 & 345 \end{bmatrix}$$

The final circular convolution result obtained by Winograd-based DFT matches the direct and DFT methods.

REFERENCES

[1] T. Pattnaik, P. Kanungo, P. K. Sahoo, T. Kar, P. Jain, M. S. Soliman, and M. T. Islam, "An efficient low complex-functional link artificial neural network-based framework for uneven light image thresholding," *IEEE Access*, vol. 12, pp. 118315–118338, 2024.

[2] G. A. Roth, G. A. Roth, D. Abate, K. H. Abate, S. M. Abay, C. Naghavi, N. Abbasi, H. Abbastabar, F. Abd-Allah, J. Abdela, A. Abdelalim, and I. Abdollahpour, "Global, regional, and national age-sex-specific mortality for 282 causes of death in 195 countries and territories, 1980–2017: A systematic analysis for the global burden of disease study 2017," *Lancet*, vol. 392, pp. 1736–1788, Nov. 2018.

[3] J. E. Sanderson, B. M. Mayosi, S. Yusuf, S. Reddy, S. Hu, Z. Chen, and A. Timmis, "Global burden of cardiovascular disease," *Heart*, vol. 93, no. 10, p. 1175, 2007.

[4] T. J. Thom, "Stroke mortality trends an international perspective," *Ann. Epidemiol.*, vol. 3, no. 5, pp. 509–518, Sep. 1993.

[5] J. Demirovic and R. J. Myerburg, "Epidemiology of sudden coronary death: An overview," *Prog. Cardiovascular Diseases*, vol. 37, no. 1, pp. 39–48, Jul. 1994.

[6] E. A. Haluska, S. J. Whistler, R. G. Baker, and R. V. Calfee, "Implantable cardiac stimulator for detection and treatment of ventricular arrhythmias," U.S. Patent 0 687 5218, Jun. 17, 1986.

[7] G. H. Bardy, W. J. Rissmann, A. H. Ostroff, P. J. Erlinger, and V. Allavatam, "Apparatus and method of arrhythmia detection in a subcutaneous implantable cardioverter/defibrillator," Tech. Rep., 2001. [Online]. Available: https://patents.justia.com/patent/6754528

[8] H. Sawaya, I. A. Sebag, J. C. Plana, J. L. Januzzi, B. Ky, V. Cohen, S. Gosavi, J. R. Carver, S. E. Wiegers, R. P. Martin, M. H. Picard, R. E. Gerszten, E. F. Halpern, J. Passeri, I. Kuter, and M. Scherrer-Crosbie, "Early detection and prediction of cardiotoxicity in chemotherapy-treated patients," *Amer. J. Cardiol.*, vol. 107, no. 9, pp. 1375–1380, Mar. 2011.

[9] R. Khurshid, M. Awais, and J. Malik, "Electrophysiology practice in low- and middle-income countries: An updated review on access to care and health delivery," *Heart Rhythm O2*, vol. 4, no. 1, pp. 69–77, Jan. 2023.

[10] M. S. Supriya, L. Yashaswini, and K. Arvind, "Exploring deep learning approaches for cardiac arrhythmia diagnosis," in *Artificial Intelligence in Medicine*. CRC Press, 2024, pp. 3–14.

[11] Y. Jin, Z. Li, M. Wang, J. Liu, Y. Tian, Y. Liu, X. Wei, L. Zhao, and C. Liu, "Cardiologist-level interpretable knowledge-fused deep neural network for automatic arrhythmia diagnosis," *Commun. Med.*, vol. 4, no. 1, p. 31, Feb. 2024.

[12] P. K. Sahoo, P. Kanungo, S. Mishra, and B. P. Mohanty, "Entropy feature and peak-means clustering based slowly moving object detection in head and shoulder video sequences," *J. King Saud Univ. - Comput. Inf. Sci.*, vol. 34, no. 8, pp. 5296–5304, Sep. 2022.

[13] E. A. Sandhya Samant, "Exploring ECG signal analysis techniques for arrhythmia detection: A review," *Int. J. Recent Innov. Trends Comput. Commun.*, vol. 11, no. 9, pp. 4881–4896, Nov. 2023.

[14] A. Rath, D. Mishra, G. Panda, and S. C. Satapathy, "Heart disease detection using deep learning methods from imbalanced ECG samples," *Biomed. Signal Process. Control*, vol. 68, Jul. 2021, Art. no. 102820.

[15] Y. Elul, A. A. Rosenberg, A. Schuster, A. M. Bronstein, and Y. Yaniv, "Meeting the unmet needs of clinicians from AI systems showcased for cardiology with deep-learning–based ECG analysis," *Proc. Nat. Acad. Sci. USA*, vol. 118, no. 24, Jun. 2021, Art. no. e2020620118.

[16] S. C. Virgeniya and E. Ramaraj, "A novel deep learning based gated recurrent unit with extreme learning machine for electrocardiogram (ECG) signal recognition," *Biomed. Signal Process. Control*, vol. 68, Jul. 2021, Art. no. 102779.

[17] G. Liu, X. Han, L. Tian, W. Zhou, and H. Liu, "ECG quality assessment based on hand-crafted statistics and deep-learned S-transform spectrogram features," *Comput. Methods Programs Biomed.*, vol. 208, Sep. 2021, Art. no. 106269.

[18] Y. Yang, M. Xu, A. Liang, Y. Yin, X. Ma, Y. Gao, and X. Ning, "A new wearable multichannel magnetocardiogram system with a SERF atomic magnetometer array," *Sci. Rep.*, vol. 11, no. 1, p. 5564, Mar. 2021.

[19] S. Din, M. K. Qaraqe, O. Mourad, K. A. Qaraqe, and E. Serpedin, "ECG-based cardiac arrhythmias detection through ensemble learning and fusion of deep spatial–temporal and long-range dependency features," *Artif. Intell. Med.*, vol. 150, Apr. 2024, Art. no. 102818.

[20] L. Jin, "ECG arrhythmia detection using disease-specific attention-based deep learning model," 2024, *arXiv:2407.18033*.

[21] Z. Ma, J. Wang, J. Yue, and Y. Lin, "A homologous and heterogeneous multi-view inter-patient adaptive network for arrhythmia detection," *Comput. Methods Programs Biomed.*, vol. 241, Nov. 2023, Art. no. 107740.

[22] B. Fatimah, A. Singhal, and P. Singh, "ECG arrhythmia detection in an inter-patient setting using Fourier decomposition and machine learning," *Med. Eng. Phys.*, vol. 124, Feb. 2024, Art. no. 104102.

[23] R. Yilmaz and F. H. Yağin, "Early detection of coronary heart disease based on machine learning methods," *Med. Records*, vol. 4, no. 1, pp. 1–6, Jan. 2022.

[24] R. Bond, D. Finlay, S. S. Al-Zaiti, and P. Macfarlane, "Machine learning with electrocardiograms: A call for guidelines and best practices for 'stress testing' algorithms," *J. Electrocardiol.*, vol. 69, pp. 1–6, Nov. 2021.

[25] J. W. Hughes, J. E. Olgin, R. Avram, S. A. Abreau, T. Sittler, K. Radia, H. Hsia, T. Walters, B. Lee, J. E. Gonzalez, and G. H. Tison, "Performance of a convolutional neural network and explainability technique for 12-lead electrocardiogram interpretation," *JAMA Cardiol.*, vol. 6, no. 11, p. 1285, Nov. 2021.

[26] A. Malali, S. Hiriyannaiah, G. M. Siddesh, K. G. Srinivasa, and N. T. Sanjay, "Supervised ECG wave segmentation using convolutional LSTM," *ICT Exp.*, vol. 6, no. 3, pp. 166–169, Sep. 2020.

[27] S. Hong, Y. Zhou, J. Shang, C. Xiao, and J. Sun, "Opportunities and challenges of deep learning methods for electrocardiogram data: A systematic review," *Comput. Biol. Med.*, vol. 122, Jul. 2020, Art. no. 103801.

[28] G. Wang, L. Yang, M. Liu, X. Yuan, P. Xiong, F. Lin, and X. Liu, "ECG signal denoising based on deep factor analysis," *Biomed. Signal Process. Control*, vol. 57, Mar. 2020, Art. no. 101824.

[29] S. Shinde and J. C. Martinez-Ovando, "Heart disease detection with deep learning using a combination of multiple input sources," in *Proc. IEEE 5th Ecuador Tech. Chapters Meeting (ETCM)*, Oct. 2021, pp. 1–3.

[30] R. Avanzato and F. Beritelli, "Heart disease recognition based on extended ECG sequence database and deep learning techniques," in *Proc. IEEE Int. Conf. Internet Things Intell. Syst. (IoTaIS)*, Nov. 2022, pp. 117–121.

[31] R. Deepika, P. B. Srikaanth, and R. Pitchai, "Early detection of heart disease using deep learning model," in *Proc. 8th Int. Conf. Smart Struct. Syst. (ICSSS)*, Apr. 2022, pp. 1–4.

[32] K. Mehta and K. Subramanian, "Heart disease diagnosis using deep learning," in *Proc. IEEE India Council Int. Subsections Conf. (INDISCON)*, Jul. 2022, pp. 1–6.

[33] P. Jain, J. Yedukondalu, H. Chhabra, U. Chauhan, and L. D. Sharma, "EEG-based detection of cognitive load using VMD and LightGBM classifier," *Int. J. Mach. Learn. Cybern.*, vol. 15, no. 9, pp. 4193–4210, Sep. 2024.

[34] F. S. Butt, M. F. Wagner, J. Schäfer, and D. G. Ullate, "Toward automated feature extraction for deep learning classification of electrocardiogram signals," *IEEE Access*, vol. 10, pp. 118601–118616, 2022.

[35] A. Siamak, R. Sadeghian, I. Abdellatif, and S. Nwoji, "Diagnosing heart disease types from chest X-rays using a deep learning approach," in *Proc. Int. Conf. Comput. Sci. Comput. Intell. (CSCI)*, Dec. 2019, pp. 910–913.

[36] A. A. Nasser and M. A. Akhloufi, "Deep learning methods for chest disease detection using radiography images," *Social Netw. Comput. Sci.*, vol. 4, no. 4, p. 388, May 2023.

[37] M. Alslatie, H. Alquran, W. A. Mustafa, I. Abu-Qasmieh, A. M. Alqudah, and A. Alkhayyat, "Automated diagnosis of heart-lung diseases in chest X-ray images," in *Proc. 5th Int. Conf. Eng. Technol. Appl. (IICETA)*, May 2022, pp. 537–541.

[38] S. Yuan, B. Wu, and P. Li, "Intra-pulse modulation classification of radar emitter signals based on a 1-D selective kernel convolutional neural network," *Remote Sens.*, vol. 13, no. 14, p. 2799, Jul. 2021.

[39] X. Hu, W. Yang, H. Wen, Y. Liu, and Y. Peng, "A lightweight 1-D convolution augmented transformer with metric learning for hyperspectral image classification," *Sensors*, vol. 21, no. 5, p. 1751, Mar. 2021.

[40] H. Gao, Z. Wang, L. Cai, and S. Ji, "ChannelNets: Compact and efficient convolutional neural networks via channel-wise convolutions," *IEEE Trans. Pattern Anal. Mach. Intell.*, vol. 43, no. 8, pp. 2570–2581, Aug. 2021.

[41] P. K. Sahoo, M. K. Panda, U. Panigrahi, G. Panda, P. Jain, M. S. Islam, and M. T. Islam, "An improved VGG-19 network induced enhanced feature pooling for precise moving object detection in complex video scenes," *IEEE Access*, vol. 12, pp. 45847–45864, 2024.

[42] A. Houkan, A. K. Sahoo, S. P. Gochhayat, P. K. Sahoo, H. Liu, S. G. Khalid, and P. Jain, "Enhancing security in industrial IoT networks: Machine learning solutions for feature selection and reduction," *IEEE Access*, vol. 12, pp. 160864–160883, 2024.

[43] H. Chhabra, U. Chauhan, P. Jain, L. D. Sharma, and A. Dev, "Machine learning assisted EEG signal classification for automated diagnosis of mental stress," in *Artificial Intelligence in Biomedical and Modern Healthcare Informatics*. Amsterdam, The Netherlands: Elsevier, 2025, pp. 447–454.

[44] U. Panigrahi, P. K. Sahoo, M. K. Panda, and G. Panda, "A ResNet-101 deep learning framework induced transfer learning strategy for moving object detection," *Image Vis. Comput.*, vol. 146, Jun. 2024, Art. no. 105021.

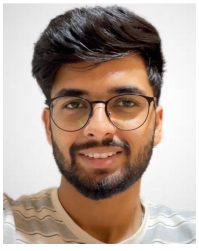

RISHABH ANAND is currently pursuing the degree in computer science engineering with C. V. Raman Global University, Bhubaneswar. His academic interests include artificial intelligence, machine learning, and signal processing. He has been actively involved in research related to machine learning and DL methodologies, contributing to projects that enhance the understanding of signals, and images, and optimizing the computational complexity of models. He aims to leverage his engineering background to advance innovations in technology and healthcare.

ADYASHA RATH (Student Member, IEEE) received the M.Tech. degree in CSE, in 2019, and the Ph.D. degree in computer science and engineering (development of intelligent models for efficient detection of heart diseases) from Siksha 'O' Anusandhan (Deemed to be) University, Bhubaneswar, Odisha, in April 2023. She is currently an Assistant Professor with the Department of Computer Science and Engineering, C. V. Raman Global University, Odisha, India. To date, she has a total teaching experience of three years and research experience of another three years. She has a number of publications in various journals and international conferences. In November 2024, her number of citations was 311, with an H-index of nine, and an i10-index of eight. She possesses a consistently excellent academic record. Her research interests include data analytics, soft computing, evolutionary computing, machine and DL techniques, and their applications to healthcare, finance, and network security. She received the Gold Medal for securing 1st position in M.Tech. She received the young technocrat award, in September 2023. She is a regular reviewer of many international journals.

PRABODH KUMAR SAHOO (Member, IEEE) received the M.E. degree from Rajiv Gandhi Proudyogiki Vishwavidyalaya, Bhopal, India, in 2005, and the Ph.D. degree from the Centurion University of Technology and Management, Odisha, India, in 2019. Currently, he is an Associate Professor with the Mechatronics Engineering Department, Parul University, Vadodara, Gujarat, India. He has contributed significantly to his field, having published fifteen peer-reviewed journal articles, presented ten international conference papers, and secured two international and one national patents. His primary research interests include image processing, computer vision, and cyber-physical systems.

PRINCE JAIN (Member, IEEE) received the Visvesvaraya Ph.D. Scheme Fellowship to complete his Doctor of Philosophy (Ph.D.) dissertation with Punjab Engineering College (Deemed to be University), Chandigarh, India. He is currently an Assistant Professor (Research Cadre) with the Mechatronics Engineering Department, Parul Institute of Technology, Parul University, Vadodara, India. He is the author and the co-author of about 60 research articles and a few book chapters on various topics related to machine learning and metamaterials. His research interests include machine learning, artificial intelligence, optimization techniques, metamaterial absorbers/antennas at RF, THz, and visible frequencies, material science, nanotechnology, and biomedical signal processing. He is serving as a Topical Advisory Panel Member for *Micromachines* and *Materials* (MDPI). He serves as an Academic Editor for *Scientific Reports Nature*, *Journal of Electrical and Computer Engineering* (Wiley), *PLOS One*, and *Discover Applied Science* (Springer). He is also working on an Extra-Mural Research Project sanctioned under the CSIR-ASPIRE scheme. He has contributed as a peer reviewer for prestigious publishers, including IEEE, Elsevier, Springer, IOPscience, Wiley, MDPI, Frontiers, PIER, Emerald, Bentham Science, and PLOS.

GANAPATI PANDA (Life Senior Member, IEEE) received the Ph.D. degree in electronics and communication engineering from IIT Kharagpur, in 1981. He did a postdoctoral research work with The University of Edinburgh, U.K., from 1984 to 1986. Currently, he is a Professor and a Research Advisor with C. V. Raman Global University, Bhubaneswar, India. He is also a Professorial Fellow with Indian Institute of Technology, Bhubaneswar. Prior to this, he was a Professor, the Dean, and the Deputy Director of the School of Electrical Sciences, IIT Bhubaneswar. He has guided 46 Ph.D. students in the fields of signal processing, communication, and machine learning.

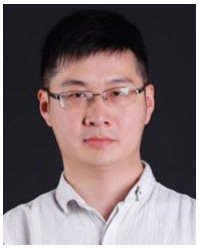

XINHONG WANG received the bachelor's degree in medical imaging technology from Sichuan University, in 2011, and the Ph.D. degree in biomedical engineering from Zhejiang University. He has been engaged in mixed research in the fields of biomedical engineering and medicine. He is currently an Associate Professor with The Second Affiliated Hospital, Zhejiang University School of Medicine. His research interests include medical imaging technology, imaging equipment development, and computational hemodynamics.

HAIPENG LIU received the bachelor's and master's degrees in engineering from Zhejiang University, China, in 2012 and 2015, respectively, and the Doctor of Philosophy degree in medical sciences from The Chinese University of Hong Kong, in 2018. From 2019 to 2020, he was a Research Fellow with the Medical Technology Research Centre, Anglia Ruskin University. From 2020 to 2024, he was a Research Fellow with Coventry University, U.K. He is currently an Assistant Professor with Coventry University, U.K. He is a Lecturer of two undergraduate course modules with Coventry University, a PI and a mentor of undergraduate student internship project of Anglia Ruskin University, an Invited Lecturer with European Institute of Innovation and Technology (EIT) Summer School and University Hospitals Coventry and Warwickshire NHS Trust, and a mentor of the National Medical Research Association (NMRA). He is the author of over 70 journal articles, 15 book chapters, and 11 conference papers, with over 1400 citations and the H-index of 20. His research interests include computational simulation of cardio-cerebrovascular diseases, AI-enhanced diagnostics, and wearable sensor development. He was a recipient of the Travel Award of British Heart Foundation, the Research and Innovation Support Fund of Anglia Ruskin University, and four Ph.D. grants from Coventry University. He is a member of the World Stroke Organization and Chinese Stroke Association. He is an editorial member of six academic journals. He is a peer-reviewer of more than 100 academic papers from over 30 academic journals, four international conferences, and two book proposals.